Additive Manufacturing 63 (2023) 103424

Contents lists available at ScienceDirect

Additive Manufacturing

journal homepage: www.elsevier.com/locate/addma

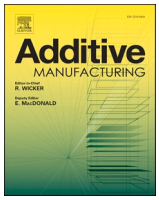

Additive manufacturing of a functionally graded high entropy alloy using a hybrid powder-bed wire-based direct energy deposition approach

Yao Lu [a,1], Jun Wang [b,*,1], Stewart Williams [b], Lisong Zhu [a], Jialuo Ding [b], Chenglei Diao [b], Zhengyi Jiang [a,*]

[a] School of Mechanical, Materials Mechatronic and Biomedical Engineering, University of Wollongong, Wollongong, NSW 2522, Australia
[b] Welding and Additive Manufacturing Centre, Cranfield University, Cranfield, Bedfordshire, MK43 0AL, United Kingdom

ARTICLE INFO

Keywords:
Hybrid direct energy deposition
Functionally graded material
High entropy alloy
Microstructure evolution
Mechanical properties

ABSTRACT

A functionally graded $Al_xCoCrFeNi$ high entropy alloy with a variation in Al concentration along the building direction was in-situ produced using a hybrid powder-bed wire-based direct energy deposition process. A continuous transition from a single FCC structure to a major BCC+minor FCC dual-phase structure was achieved, benefiting from the remelting and reheating process during the deposition. In the FCC→BCC transition zone, the dendritic core region is identified as an FCC matrix decorated by AlNi-rich ordered B2 precipitates. The inter-dendritic area shows B2 precipitating in the FeCr-rich disordered A2 matrix. Additionally, the interface between the two regions shows that the A2 phase and ordered Cr_3Fe intermetallic phase precipitate at the B2 phase. The mechanical properties show a tendency for higher strength and hardening rate but lower plasticity corresponding to the areas with higher Al content. Through quantitative estimation of different strengthening mechanisms, the contribution from precipitation strengthening became increasingly apparent as Al content increased. Other strengthening modes, including solid solution and dislocations, also contribute to the total strength. This investigation realises a novel additive manufacturing method combining powder bed and wire feeding, which can produce a more convenient and cost-effective gradient material with a complex composition.

1. Introduction

The 21st century has witnessed the widely accepted concept of high entropy alloying in designing and processing compositionally unbiased materials (high entropy alloys, also called HEAs), which is beyond the traditional single-element-dominated alloy systems [1,2]. Since a high mixing entropy stabilises a solid-solution state, simple solid solution phases (face-centred-cubic, FCC or body-centred-cubic, BCC) instead of intermetallic compounds usually appear in HEAs. This innovative approach could make HEAs realise unique performance advantages in a similar composition, including outstanding strength and toughness both at ambient and hypothermia [3,4], excellent resistance to wear and corrosion [5,6], and perfect thermal stability [7–10]. As one of the most comprehensively investigated HEA systems, the $Al_xCoCrFeNi$ HEA system has gained increasing research interest fascinated of its prominent match of mechanical and functional performances [11], abundant constitutive elements with low cost [12], and the capability of modifying phase composition merely through adjusting the addition of Al content [13]. Low Al proportion ($x<0.5$) facilitates the formation of a single FCC phase, and gradually increased content of Al ($0.5 \leq x \leq 0.9$) in the $Al_xCoCrFeNi$ system induces the formation of BCC structure with accumulated proportion. This duplex structure will adopt a predominant BCC structure as the Al atomic ratio increases [11]. Therefore, such remarkable phase flexibility realised by compositional variation in the $Al_xCoCrFeNi$ system may generate a supernormal microstructure and performance design tunability.

Functionally graded materials (FGMs) with continuous space transition of microstructure or composition within a single component are emerging to be a new generation of innovative materials, which possess extraordinary abilities to be tailored to specific requirements or performances [14]. Different from conventional composite materials, interfaces are well distinguished between different zones in FGMs, precisely contributing to the reduction of stress concentration in mechanical and thermal terms [15]. Attention to FGMs has recently

* Corresponding authors.
E-mail addresses: Jun.Wang.123@cranfield.ac.uk (J. Wang), jiang@uow.edu.au (Z. Jiang).
[1] Co-first author.

https://doi.org/10.1016/j.addma.2023.103424
Received 26 October 2022; Received in revised form 19 December 2022; Accepted 21 January 2023
Available online 23 January 2023

increased because of their high possibility to produce materials with tailored properties appropriate for many high-tech applications, e.g., nuclear, bio-engineering and aerospace industry [16]. In FGMs, the energy "disruptors" and "absorbers" are based on the force/energy interaction with the material used for impact applications [17]. "Absorbers" convert kinetic energy to lower types of energy and thus could withstand substantial plastic deformation before failure. In contrast, since "distractors" consist of high-strength material, they tend to be applied as energy transfer. Accordingly, the composite of these two factors could obtain superior impact properties because the hard part prefers to resist deformation while the tough part absorbs energy and prevents cracks [18]. Inspired by this notion, HEA FGM is starting to come into view, including $Al_xCoCrFeNi$ and $V_xAlCrFeMo$ [17,19]. Since Al addition in HEAs could stabilise the BCC phase and form a passive oxide layer, therefore, $Al_xCoCrFeNi$ FGM could achieve a unique spacial feature of a ductile end passing to a hard and oxidation-resistant end with a continuous transition, which has great potential in the extreme working environment, such as aerospace. In addition to the metallurgical bond, the traditional material preparation process also requires massive machining, and post-heat treatment, leading to the whole process being more complicated and lengthier. Therefore, the possibility of employing new manufacturing technology to prepare gradient materials is worth exploring.

Additive manufacturing (AM) as a manufacturing technique has attracted plenty of attention in producing metallic materials due to its capability of directly producing complex-shaped components, reducing the post-machining and assembly steps [20]. Two categories can be classified in AM technologies: powder bed fusion (PBF) and directed energy deposition (DED). Compared with PBF, the DED technique exhibits distinct advantages, including high deposition efficiency and cost savings [21]. Especially, the wire-DED (W-DED) technique is more suitable for heavy industries, including automobiles, aerospace, and mechanical equipment, compared with the powder-based DED. It is worth noting that in recent years, interest in employing AM to manufacture HEAs has increased significantly [22]. Under the desired processing condition, selective laser melting, as one of the PBF technologies, has been successfully employed to produce HEAs including single FCC HEA (e.g. CoCrFeMnNi), FCC+BCC dual-phase HEA (e.g. $Al_{0.2}Co_{1.5}CrFeNi_{1.5}Ti_{0.3}$), and single BCC HEA (e.g. NbMoTaW) with excellent properties and high-dimensional accuracy, e.g. [23,24,25]. In addition, selective electron beam melting has been verified to be a suitable PBF technique for producing homogeneous HEA components, including single FCC, single BCC and dual-phase HEAs, due to its high beam deflection speed and input power [26–29]. At the same time, a dramatic increase in utilisation in the production of HEAs has been achieved by other laser-powder-based DED technologies like laser-engineered net shaping and laser metal deposition [30,31,32]. However, there are very few investigations regarding the arc W-DED of HEAs. Very recently, Wang et al. [33] and Shen et al. [34] first manufactured CoCrFeNiMn HEA and $CoCrFeNi(SiC)_x$ HEAs with satisfactory formability by powder-bed arc additive manufacturing (PB-AAM), which proved the feasibility of manufacturing HEA alloys by using arc as the heat source during AM process. The $Al_xCoCrFeNi$ HEA system, as the focus of current studies, has only been realised through laser deposition methods [35,36,37], while no W-DED is reported. Even though the W-DED approach favours superiorities of high deposition rate and low cost, it is still challenging to use W-DED to in-situ manufacture HEA alloys due to the composition complexity. Therefore, this study raises a novel hybrid powder bed-wire direct energy deposition (PB-WDED) method to take advantage of powder bed fusion and W-DED.

Thus, this investigation aims to deposit $Al_xCoCrFeNi$ HEAs with a designed composition gradient achieved by the PB-WDED method and to explore the microstructural and mechanical evolution with the change of Al concentration along the building direction (BD).

2. Experimental

2.1. Raw materials and manufacturing process

A mild steel plate with dimensions of 300 × 100 × 10 mm^3 was used as the substrate. An equimolar mixture of four coarse elemental powders (Fe, Co, Cr, Ni) with technical purity over 99.5 % and particle size distribution of 300–500 μm was achieved by mechanical stirring for 1 h in an 88 mixer (system Schatz). 1080 pure Al wire with a diameter of 0.9 mm was fed into the melt pool with controlled wire feed speed as the source of Al in the functionally graded HEA component.

The functionally graded $Al_xCoCrFeNi$ high entropy alloy thin-wall bulk was manufactured on a custom-made PB-WDED system equipped with a gas tungsten arc power source and torch, a motion system with a powder bed system on top, a local shielding apparatus, a cooling unit, and a wire feeder, as shown in Fig. 1(a). The physical details are shown in Fig. 1(b1-b2), displaying the spatial relationship between the torch, wire feeder, and powder bed in this PB-WDED system. The deposition parameters displayed in Table 1 are chosen to avoid macro defects, minimise oxidation and refrain from blowing the powder outside the bed [33]. Prior to each layer deposition, the mixing (Fe, Co, Cr, Ni) powders were poured into a hollow powder holder with a thickness of 1 mm. During deposition, the Al wire was fed into the molten pool simultaneously with different feeding speeds varied with layers (See Table 2) as a supply of Al element. The gradient Al composition in the $Al_xCoCrFeNi$ FGM system can be achieved by changing the Al wire feed speed. To achieve homogeneity in structure and composition, the deposit was remelted by the heat source with the same current value immediately followed by natural cooling of every layer [33]. The as-deposited bulk component possesses a dimension of 130 mm × 25 mm × 10 mm (length × height × width) after the removal of loose powder, with the chemical compositions varied along the BD, as shown in Fig. 1(c).

2.2. Characterisation

A cross-sectional sample with a thickness of 2 mm was extracted from the middle part in the BD-ND plane of the as-deposited thin-wall structure for the microstructural and compositional examination. The macro morphology is shown in Fig.S1, and no macroscopic defects can be observed in the sample interior. The sample was ground and polished, followed by standard preparation procedures for HEA alloys, and then electro-polished at 20 V for 120 s on an electrolytic machine (Struers Lectropol 5). The evolution in microstructure and crystallographic orientation were examined with a field emission gun scanning electron microscope (SEM, JEOL JSM7001 F) equipped with Energy-dispersive X-ray spectroscopy (EDS) and electron backscattered diffraction (EBSD) detectors. During the EBSD scanning, the accelerating voltage, probe current, working distance, binning mode, and step size were set as 15 kV, 6.5 nA, 15 mm, 4 × 4, and 0.75 μm, respectively. The EDS and EBSD data were then post-processed using Aztec and AztecCrystal software, respectively. To identify the in-depth microstructure in the transition region, a foil specimen with dimensions of 10 μm × 5 μm was extracted in the transition region from the cross-sectional sample using a dual-beam Focussed Ion Beam microscope (FIB, FEI Helios NanoLab G3 CX) for further detection on a scanning transmission electron microscope (STEM, JEOL ARM 200 f). Gatan Microscopy Suite® and CrysTBox software [38] was used to analyse the STEM results. XRD and mechanical detection were conducted perpendicular to the BD instead of parallel due to the more uniformity of microstructure and composition, as shown in Fig. 1(b). The bulk samples with dimensions of 10 mm × 10 mm× 1.5 mm were extracted from the horizontal plane (ND-TD) at heights of 5, 10, 15, and 20 mm, referred to as regions I, II, III, IV, respectively, for phase identification. The phase identification of the samples was further analysed on an X-ray diffractometer (XRD, GBC MMA) with CuK α radiation (λ = 1.5418 A). The scattering angle range,

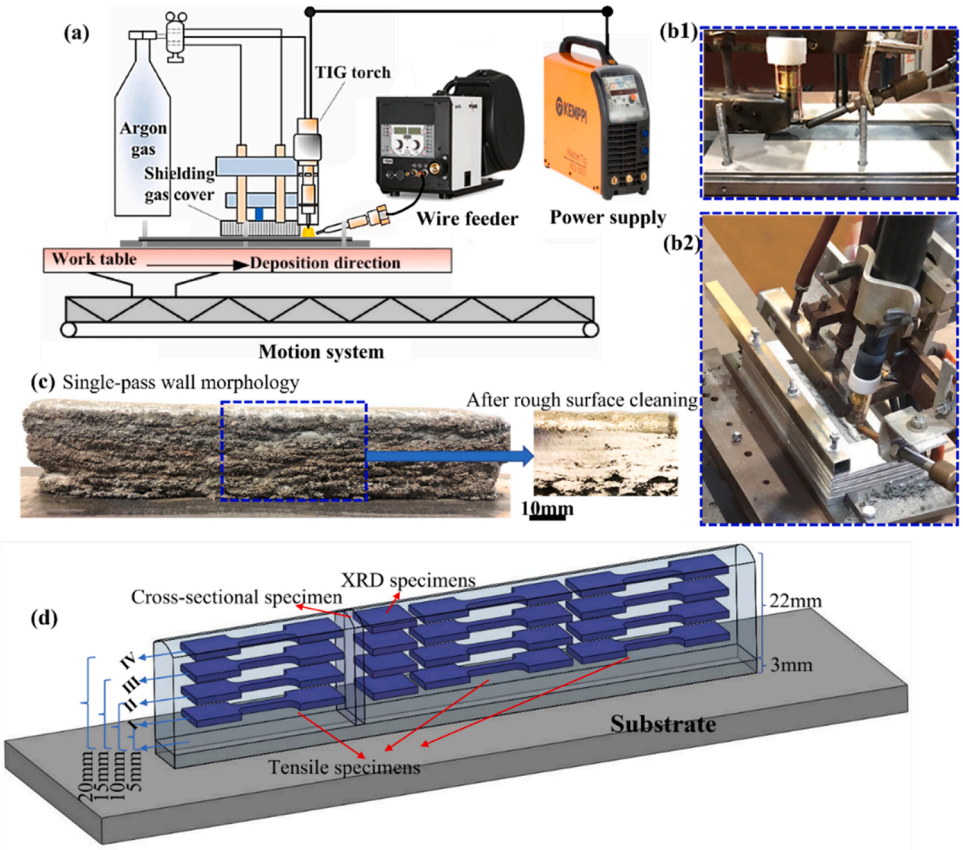

Fig. 1. (a) Schematic illustration of the hybrid powder bed-wire direct energy deposition (PB-WDED) setup; (b1, b2) detailed figure shows the relationship between torch, wire feeder, and powder bed in the PB-WDED system; (c) surface morphology of the single-pass Al_xCoCrFeNi graded high entropy wall structure; (d) extraction location of the cross-sectional specimen, XRD specimens, and tensile samples.

Table 1
Deposition processing parameters used to produce the functionally graded Al_xCoCrFeNi high entropy alloy thin-wall structure.

Parameters	Value
Torch travel speed	45 mm/min
Bead length	130 mm
Arc length	3.5 mm
Shielding gas flowrate	9 L/min
Post flow duration	90 s
Interpass cooling waiting duration	300 s
Number of deposition layers	25 layers

Table 2
Variation in the Al wire feed speed with the deposition layers.

Layers	Wire feed speed of Al (mm/min)	Expected Al content (at %)
1–5	0	0
6–9	150	3
10–13	200	6
14–17	300	9
18–21	400	12
22–25	600	18

scanning speed, and step size were set as 30° − 90°, 1°/min, and 0.02°, respectively. 3 tensile specimens with a gauge size of 10 mm × 2 mm × 1.5 mm were extracted from the horizontal plane at the same heights as the XRD samples. The tensile tests were conducted at room temperature on an Instron 8801 tensile testing unit at a constant strain rate of 10^{-3}/s.

3. Results

3.1. Composition transition along BD

The chemical composition transition along the BD of the as-deposited cross-section specimen was obtained by SEM-EDS detection with a

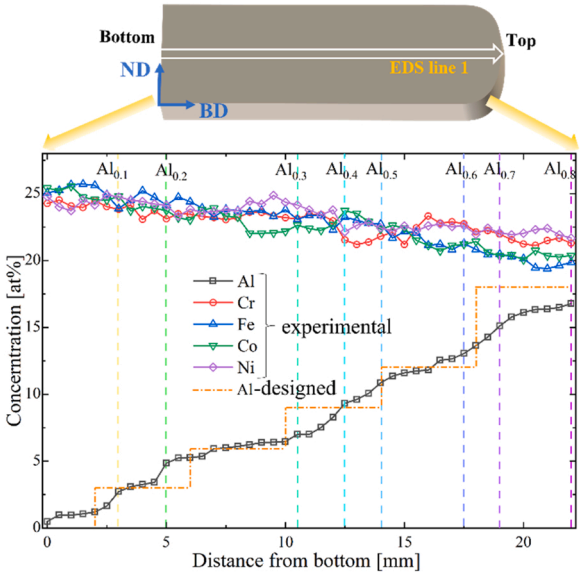

Fig. 2. Composition transition checked at the central line along BD of Al_xCoCrFeNi HEA functionally graded component deposited by PB-WDED method.

distance interval of 0.5 mm, as illustrated in Figs. 2 and S2. An area of 500 μm × 50 μm in each location instead of a point was selected to measure the composition to ensure the data reliability. The concentration of Al from the bottom (3 mm away from the fusion line to avoid the dilution effect from the substrate) to the top surface gradually increased to approximately 17 at %. Co, Cr, Fe, and Ni concentrations have a downward trend with fluctuations from 25 at % to around 21 at % with a deviation of 1 at %. Although the Al content was designed to be progressively added every four layers in a stepwise mode, in reality, a comparatively continuous transition with slight fluctuations was found in chemical composition because of the remelting and reheating process used during the deposition. Each new layer was deposited and then remelted, meaning that the upper part of the previous layers was remelted, and the lower portion was reheated, undergoing a secondary solid-phase transition [39]. This remelting and reheating process also diluted the sudden composition gradient of Al, making the transition smoother instead of stepwise.

3.2. 3.2 Phase evolution with varying Al concentration

To clarify the phase evolution along the BD, the XRD patterns obtained in different regions are shown in Fig. 3(a). After normalisation and calibration, several distinct peaks pointing to either FCC solid-solution phase (PDF: 33–0397) or BCC solid-solution phase (PDF: 54–0331) can be identified in the 2θ range of 30–90°. Elemental concentrations corresponding to approximate composition and phase constitution at these heights are summarised in Table 3. Both region I ($Al_{0.2}$CoCrFeNi) and region II ($Al_{0.28}$CoCrFeNi) exhibit a stable solid-solution FCC single phase with peaks referring to (111), (200) and (220). A stronger intensity was observed on the (200) peak compared with other peaks in both conditions, indicating a prominent [100] texture for the horizontal plane transverse to the BD. This also indicates a preferential crystal growth along the BD since grains always grow along the maximum heat flow direction at the solid-liquid interface, which is closely aligned to the BD in AM deposition process [40]. With an increasing amount of Al, a (200) reflection near 2θ ≈ 65°, a (100) reflection near 2θ≈ 30°, and a (110) reflection in the vicinity of (111) FCC peak indicate a BCC structure formed in the region III with an approximate composition of $Al_{0.53}$CoCrFeNi. A (100) reflection with comparatively weak intensity is an ordered BCC, which is a kind of B2 superstructure [13]. The difference in morphology between these two BCC structures was then investigated via SEM and STEM. It's worth noting that with a further increase in Al content at region IV ($Al_{0.76}$CoCrFeNi), the intensity of $(200)_{BCC}$ reflection was maximum among all the peaks, indicating the BCC structure replaces the FCC as the dominant phase and a strong (200) BCC texture parallel to BD. Despite this, the intensity of the $(100)_{ordered\ BCC}$ reflection has not changed significantly. Furthermore, the peak shift can be observed in FCC and BCC reflections by narrowing the angle range, as shown in Fig. 3(b–d). To be specific, the shift of the $(200)_{FCC}$ peak obviously points towards the lower 2θ side with the increase of Al concentration. This suggests an expanding trend in the interplanar spacing of the FCC structure resulting from the more significant atomic size effect of Al [13]. However, it can be found that in the dual-phase state, no matter FCC or BCC structure, the peak deflection is minimal with increased Al addition. These trends will directly affect the variation in lattice parameters of the corresponding structures. As can be seen from Fig. 3(e), the FCC lattice parameter experienced a sharp increase to a peak value of 3.614 Å at the approximate composition of $Al_{0.53}$CoCrFeNi (region III) and remained the same even though the Al level continues to rise. In contrast, just a slight increase can be observed in the lattice parameters of both the ordered and disordered BCC structures with the increment of Al content in the FCC+BCC dual-phase region. The phenomenon that lattice parameters of no matter FCC or BCC varied little in the dual-phase region could be attributed to the almost unchanged chemical compositions of FCC and BCC phases despite the constantly varied relative proportion [13].

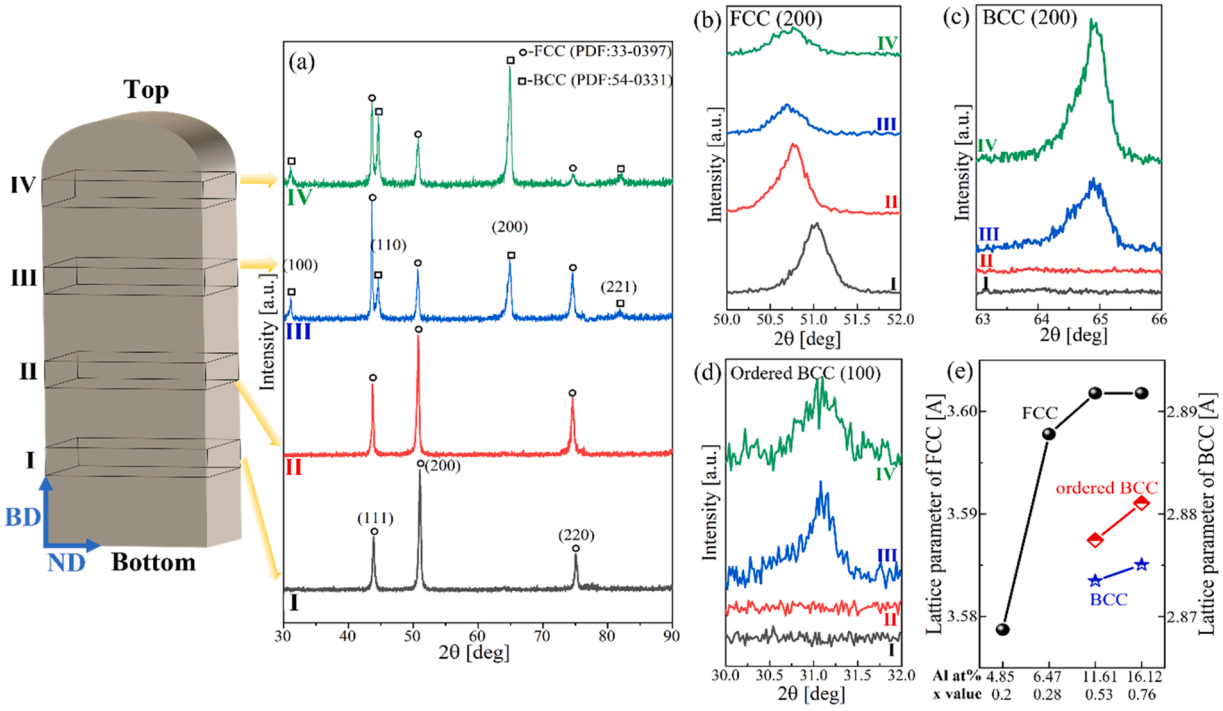

Fig. 3. (a) XRD patterns with 30°~90° 2θ range of different regions acquired at different heights of Al_xCoCrFeNi HEA graded component deposited by PB-WDED method; narrowed 2θ range showing the shift of reflections: (b) FCC (200); (c) BCC (200) and (d) ordered BCC (100); (e) lattice parameters of the FCC and BCC phases at different regions of the Al_xCoCrFeNi FGM as a function of Al content or x value.

Table 3
Chemical concentration and approximate composition measured by SEM-EDS and corresponding phase constitution obtained by XRD in the regions at different heights.

Regions		I (5 mm height)	II (10 mm height)	III (15 mm height)	IV (20 mm height)
Elemental concentration (at %)	Al	4.85	6.47	11.61	16.12
	Co	23.74	22.18	22.42	20.04
	Cr	23.12	23.2	21.2	21.24
	Fe	24.16	23.8	22.18	20.15
	Ni	24.13	24.36	22.59	22.04
Approx. composition		$Al_{0.2}$CoCrFeNi	$Al_{0.28}$CoCrFeNi	$Al_{0.53}$CoCrFeNi	$Al_{0.76}$CoCrFeNi
Phase constitution		FCC	FCC	FCC+minor BCC	BCC+minor FCC

3.3. Mechanical performance evolution with varying Al content

The tensile stress-strain curves obtained from different regions of the PB-WDED Al_xCoCrFeNi HEA FGM component are shown in Fig. 4(a). The relationship between the averages of the tensile properties, including ultimate tensile strength (UTS), yield strength (YS), elongation (EL) and corresponding local composition, are shown in Fig. 4(b). Distinct changes can be seen in UTS, YS, and EL values along BD of the FGM structure, determined by the Al concentration. The UTS, YS, and EL in the region I with a composition of $Al_{0.2}$CoCrFeNi are determined to be 537 ± 47 MPa, 365 ± 37 MPa, and 26.6 ± 5.6 %, respectively. Region II with slightly higher Al content ($Al_{0.28}$CoCrFeNi) showed comparatively higher UTS, while the YS and EL values are basically at a similar level. Since both region I and region II are located in the single-FCC phase region, it is no wonder that adding Al atoms will only contribute to a slight strengthening [13]. As the amount of Al atoms increases further, a marked increase in strength and a relative decrease in plasticity can be observed in region III with a composition of $Al_{0.53}$CoCrFeNi located in the dual FCC+BCC zone. When it comes to the mechanical performance of region IV (composition-$Al_{0.76}$CoCrFeNi; phase-BCC+FCC), a further elevation in strength and a remarkable deterioration in ductility occurred. The explanation, combined with the trend in composition and phase constitution discussed above, is that regions with a higher strength but a lower ductility correspond to the counterparts with a higher Al content and an accumulation of BCC phase. As a strong BCC stabiliser, the increasing Al content facilitates the nucleation and growth of the BCC phase both in intragranular and intergranular sites, explaining the upward trend in strength and the downward trend in ductility along BD [41]. To clarify the transition in hardening behaviour along BD as increased Al content, the plots of true stress versus true strain, and work hardening rate (WHR) versus true strain are presented in Fig. 4(c) and (d). The uniform elongation ε_u in different regions can be obtained by determining the intersection of the two curves. In comparison, the ε_u values in single FCC regions are obviously higher (22.1 % in region II, 20.7 % in region I) and will experience a substantial decline with the increase of BCC proportion

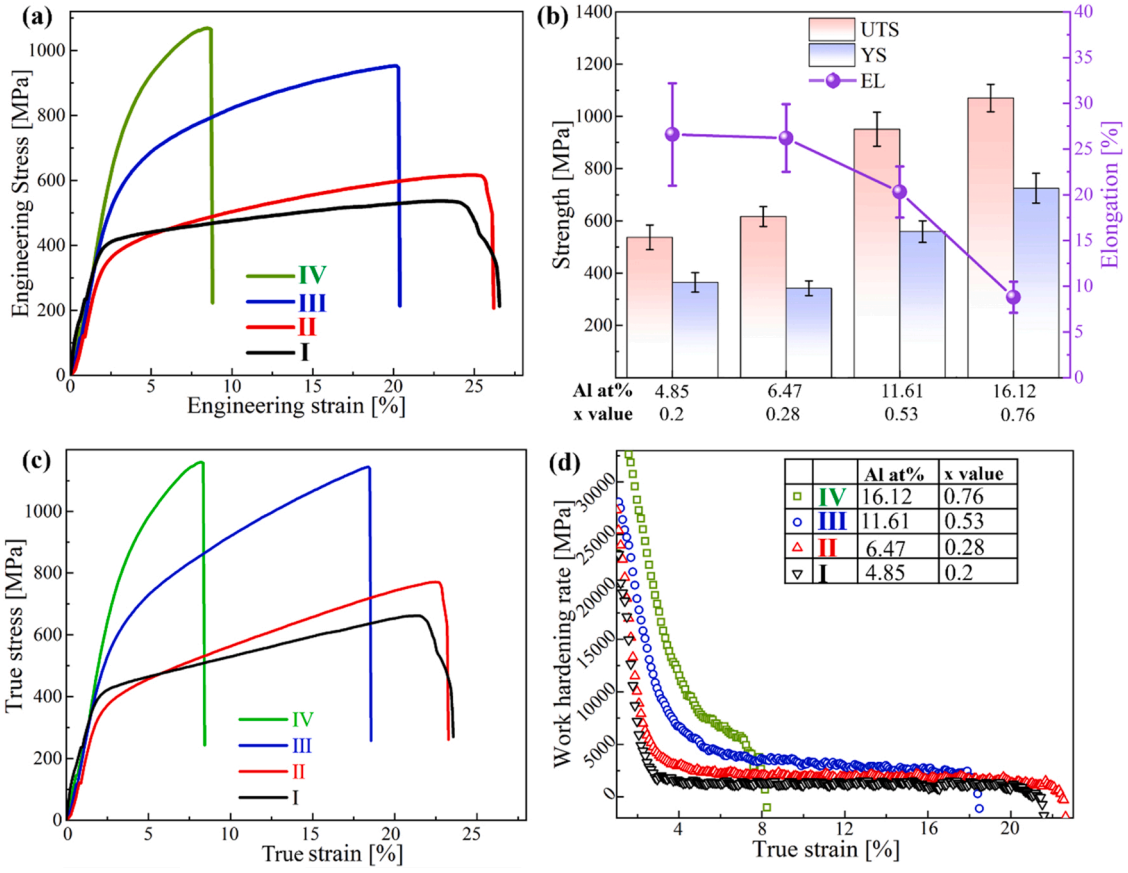

Fig. 4. Representative engineering stress-strain curves of tensile specimens obtained from different heights of the PB-WDED Al_xCoCrFeNi HEA gradient component; (b) corresponding 0.2 %-offset yield strength (YS), ultimate tensile strength (UTS), and elongation (EL) data; (c) corresponding true stress-strain curves (d) corresponding work hardening rate versus true strain curves.

when entering the dual phase regions (18.2 % in region III, 8.1 % in region IV). In terms of WHR curves, region IV with a composition of $Al_{0.78}CoCrFeNi$ shows a monotonically declined strain hardening rate while the other regions exhibit a sharply decreasing strain hardening rate after yielding and then kept almost at a similar rate level. When it comes to the strain-hardening plateau region, the strain-hardening rate in regions I, II, III, and IV were determined to be around 1260 MPa, 1840 MPa, 3320 MPa, and 6750 MPa, respectively. Furthermore, the true strain range corresponding to the plateau is significantly narrowed with the increment of Al content. Undoubtedly, a higher Al alloying in $Al_xCoCrFeNi$ HEA contributes to both the intensification of work hardening and contraction of the hardening plateau. A greater strain hardening rate undoubtedly implies more barriers to dislocation movement, leading to an enhancement in the deformation strength [42]. Also, the BCC+FCC duplex phases have enhanced dislocation storage capacity, resulting in exceptionally high work hardening [43]. The fracture mechanism in different regions of the $Al_xCoCrFeNi$ HEA FGM is also Al content dependent and discussed in supplementary S3 due to the length limitation. In general, single FCC regions (I and II) showed a typical ductile fracture feature, while dual FCC+BCC regions (IIIand IV) displayed a mixed transgranular-intergranular fracture and quasi-cleavage fracture. Also, the twin structures in the failure tensile specimens are checked by EBSD, and the results are listed in supplementary S4. Less than 0.5 % <111> 60° twin boundaries (TB) can be found in regions I-III after fracture, resulting from the extra coarse undeformed grain structures. However, the proportion of TBs in region IV after fracture is around 11 %. This is because the stacking fault energy (SFE) will be significantly reduced by the elemental partitioning between the BCC/B2 phase and FCC matrix, which will facilitate the partial dislocation mediation, leading to the formation of deformation TB in the matrix [44].

3.4. Microstructure evolution along BD

To investigate the effect of Al content variation on microstructure evolution and to further understand the evolution in mechanical properties with varying Al content, the microstructure was observed point by point along the BD. Three different zones can be clearly observed, including a single FCC zone varying from bottom to middle, a dual FCC+BCC zone, and a single BCC zone located at the very top region of the component. The microstructure and phase composition in the lower and very top regions of the FGM wall structure were examined and are compared in Fig. 5. In the lower part with an approximate composition between $Al_{0.2}CoCrFeNi$ and $Al_{0.3}CoCrFeNi$ (Fig. 5(a1, a2)), the microstructure consists of extra coarse columnar FCC grains with anisotropy closely aligned at the <001> BD, which is typically observed in additively manufactured cubic metallic materials [40]. This is because the grain orientation is highly influenced by the size and morphology of the melt pool, and the crystal growth is generally along the direction of thermal dissipation, which is perpendicular to the liquidoid/solidoid interface [45]. Nevertheless, at the top region with an estimated composition range of $Al_{0.8}CoCrFeNi$ and $Al_{0.9}CoCrFeNi$, the microstructure is composed of comparatively finer columnar BCC grains with a smaller aspect ratio, as depicted in Fig. 5(b1, b2). Also, the <100> orientation parallel to BD is becoming less preferential in this region due to the fewer reheating cycles experienced during the last few layers' depositions.

Unlike FCC columnar crystals in the lower-mid part, some substructures could be observed in the BCC grain interior in the top region, as shown in Fig. 6(a). By magnifying, it can be seen that a combination of interwoven, short-rod, and long-strip structures with a width range of 80–200 nm in a bright colour is embedded in the dark matrix. Such structures within the BCC crystals can be identified as A2 (disordered BCC) and B2 (ordered BCC) phases, conforming to the spinodal decomposition mechanism [46,47]. It has been reported that the A2 phase forms these bright precipitating domains inside the B2 matrix [48]. The morphology of the A2 and B2 phases is influenced by the lattice misfit between the precipitates and matrix. The nano-phase morphology can be altered in the following ways under the influence of gradually increasing lattice mismatch: coherent spherical → coherent cube → coarsening until incoherence. Here, the spinodal morphology of A2 and B2 coherent phases, corresponding to a comparatively larger lattice mismatch, may exert a detrimental effect on mechanical performance [49]. Additionally, the corresponding alloy elements distribution was obtained by the EDS map and line scan, as shown in Fig. 6(c) and (d), respectively. Clearly, Fe and Cr can be identified to be rich in the A2

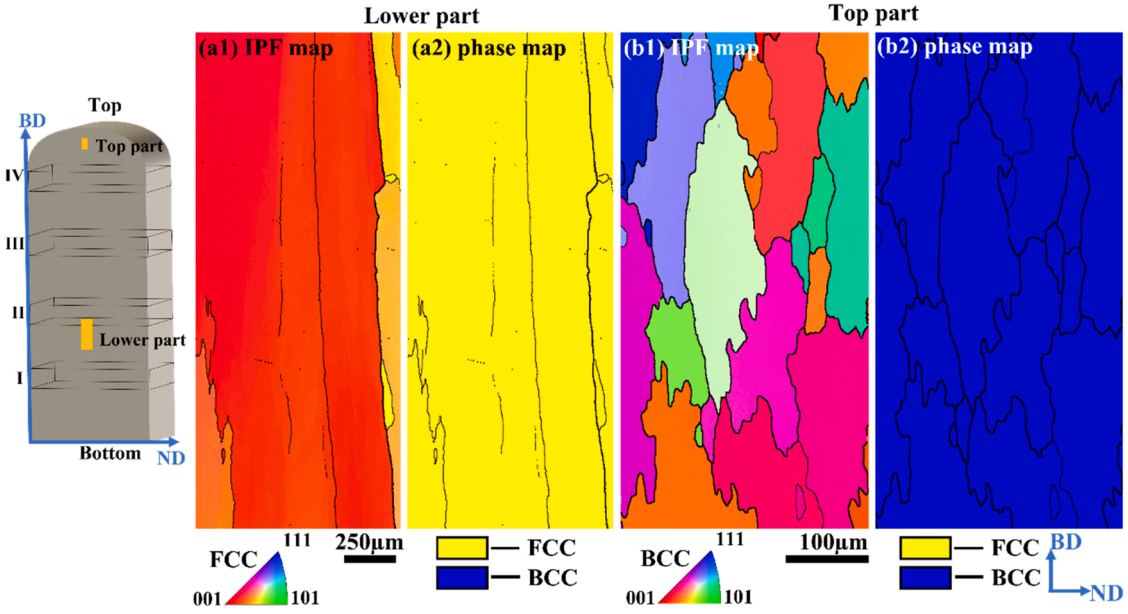

Fig. 5. EBSD orientation maps and phase maps of the PB-WDED $Al_xCoCrFeNi$ HEA FGM component taken at the lower and top parts are displayed in (a1-a2) and (b1-b2), respectively. The crystal orientation–colour relation map corresponds to the inverse pole figure (IPF) legend. The FCC phase was highlighted in yellow, while the BCC phase was marked in blue. Note that the relationship between sampling and coordinates (building (BD), normal (ND), and transverse (TD) directions) are indicated on the right bottom.

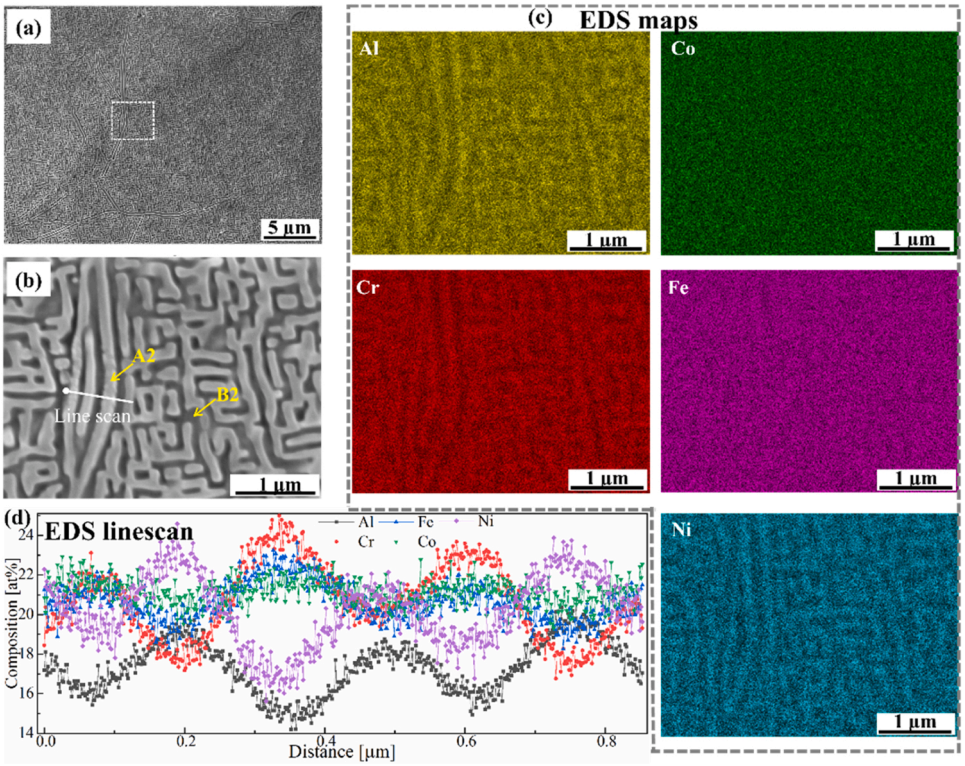

Fig. 6. SE images taken at the top region with magnifications of (a) 4000× and (b) 30,000×, and corresponding alloy elemental distributions in the region shown in (b): (c) EDS maps; (d) EDS line scans indicated in (b).

domains, while Ni and Al are rich in the B2 matrix. By comparison, Co does not show significant segregation in either A2 or B2 domains. The nanoscale substructure of coherent FeCr-rich A2 and NiAl-rich B2 has been previously reported in Ref. [50,51].

With the increase of Al concentration, the single-FCC region gradually transits to the FCC+BCC dual-phase region, and a major part of this region can be seen in Fig. 7. This dual-phase zone has a total span of around 7 mm in BD, starting at 8.5 mm and ending at 1.5 mm far away from the top. At the very top region, a BCC single-phase zone can be identified. As can be seen from the BC (band contrast) map shown in

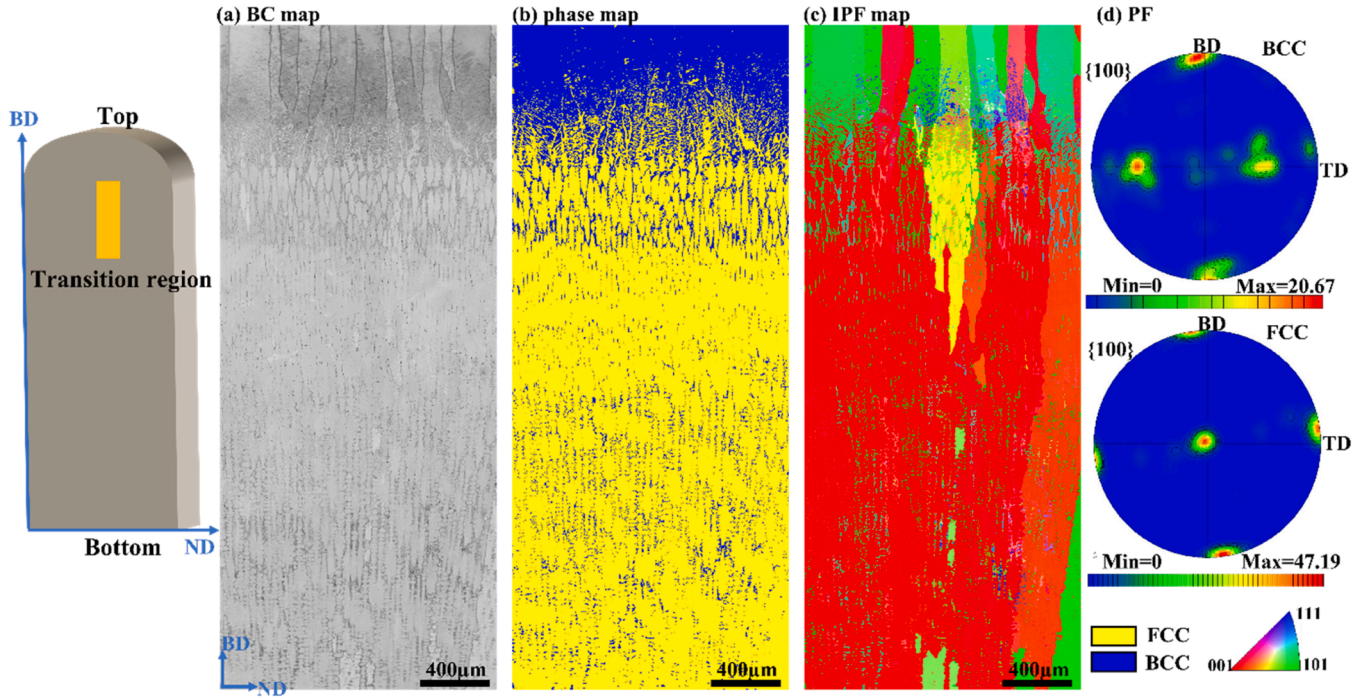

Fig. 7. EBSD scan results taken at the transition region from FCC to BCC in the BD-ND plane: (a) BC (band contrast) map; (b) phase map with FCC phase in yellow colour and BCC phase in blue colour; and (c) IPF map; (d) PFs (pole figures) of BCC and FCC phases. The scale of the figures and the legend for IPF concerning the crystal orientation–colour relation map are illustrated in the lower right corner. Note that the BCC and B2 phases cannot be differentiated by EBSD.

Fig. 7(a), from the bottom to the top of the transition part, the columnar crystal size varies from the millimetre level to the hundred-micron scale, with dendrites inside changing from dispersing to forming a network. It can be seen from the phase map (Fig. 7(b)) that the millimetre grain is mainly FCC in yellow and the hundred-micron grain is BCC in blue. With the increase of Al content, the BCC dendrites gradually grow upwards, converge into a network, and form BCC columnar grains. The EBSD orientation map (Fig. 7(c)) shows that the growth direction of the FCC columnar closely aligns with the <001> BD while the counterpart of BCC turns to track <101> BD. The <100> BD is well known in respect of being the most favourable grain growth direction in AM-deposited cubic materials, paralleling the direction of the steep temperature gradients [51]. The {100} pole figures (PFs) for FCC and BCC phases were constructed from the EBSD data, as displayed in Fig. 7(d). The major axis orientation was tilted less than 5° from BD for both cases. The maximum pole intensity for FCC and BCC can be identified in the tilted {100} <001> cube and {110} <001> Goss texture. Both the {100} <001> and {110} <001> belong to the recrystallisation texture paralleling BD. The repeated remelting and reheating in the PB-WAAM process is analogous to an annealing treatment, consequently, inevitably bringing about recrystallisation.

The microstructure evolution in the dual-phase transition region from FCC to BCC is shown in Fig. 8 from low magnification progressively to higher magnification. The upper part of the transition zone at a magnification of 200× is shown in Fig. 8(a), implying the FCC+BCC dual phase transitioned to BCC monophase. In the upper zone of Fig. 8 (a), the dark dendrites grow along BD and are embedded in the light matrix. By magnifying, the secondary dendrites with an island structure can be observed (Fig. 8(b)). Combined with the above phase analysis, these primary and secondary dendrites in dark contrast are identified as the FCC phase while the light matrix belongs to the BCC phase. Zooming in further (Fig. 8(c-d)), a wave-like substructure can be observed inside the BCC matrix. The corresponding EDS mapping results shown in Fig. 9 (a) indicate that the FCC dendrites are rich in Fe and Cr, while the BCC matrix is rich in Ni and Al. By contrast, the distribution of Co is relatively uniform in both FCC and BCC regions. By amplifying the lower-middle zone in Fig. 8(a), the dark biconical FCC substructure with light BCC dendrites decorated at the cell boundaries can be observed (shown in Fig. 8(e)). The long axes of these biconical cellulars are aligned with the BD. Zooming further specifies the BCC morphologies of partially joined dots and short rods, as shown in Fig. 8(f-h). Notably, quantities of short-rod-like precipitates are distributed within the FCC substructure, ranging in length from approximately 200 nm to 1 μm. The EDS mapping analysis on this area shown in Fig. 9(b) indicates that these precipitates are Al-depleted but Cr-rich compared with their matrix. There are two possible explanations for this precipitate: 1) it is a third crystal structure apart from FCC and BCC due to its Al-depleted characteristic; 2) it could be cratered remaining from BCC precipitates which were pulled out during the metallographic preparation process. STEM analysis is used to identify it, which will be discussed later. The lower part of the transition region shown in Fig. 8(h) exhibits a typical dendritic structure. It is quite similar to the one displayed in Fig. 8(e), showing a

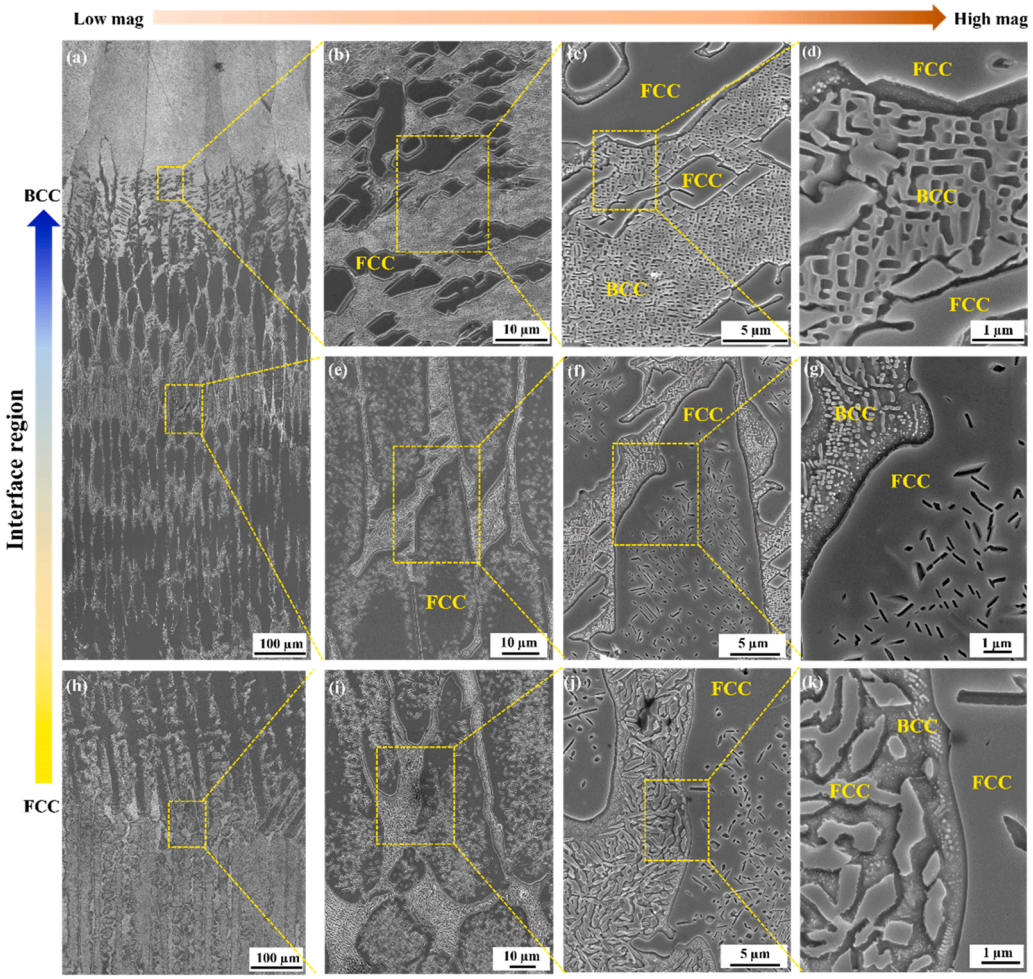

Fig. 8. SE images at different magnifications of the interface region showing dendritic morphology: (a) upper part of the interface region; (b-d) progressively enlarged SE images exhibiting the FCC dendrites embedded in the BCC matrix, (e-g) gradually magnified SE images depicting the BCC dendrites and FCC inter-dendrites; (h) lower-middle part of the interface region; (i-k) stepwise magnified SE images showing morphology details in (h).

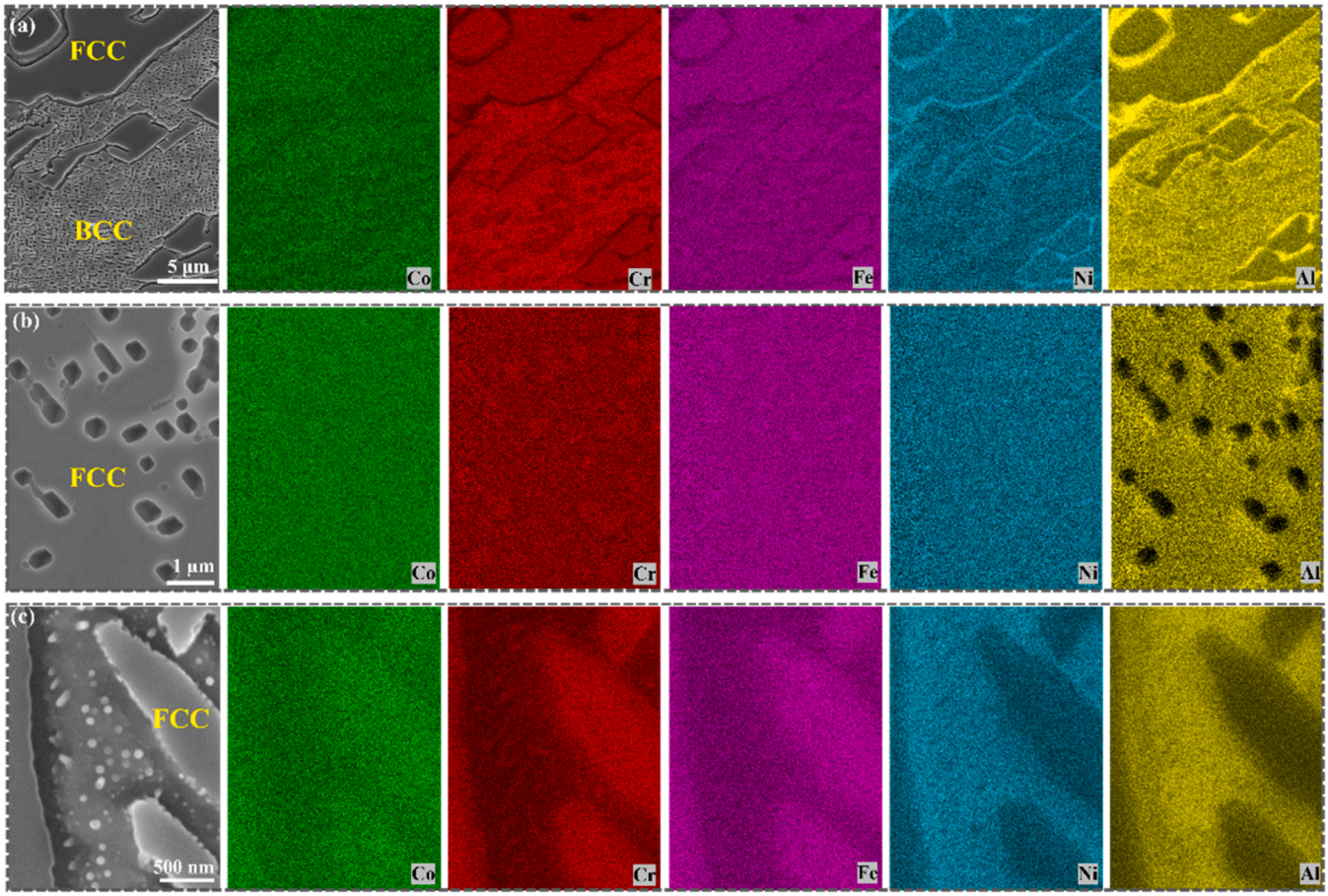

Fig. 9. EDS mapping results showing elemental distributions taken at different zones in the transition region: (a) corresponds to Fig. 8(c); (b) corresponds to a portion of Fig. 8(g); (c) corresponds to a portion of Fig. 8(j).

cell structure with precipitates inside and intercellular dendrites. Fig. 8 (i-k) shows that the short rod-like structures inside the intercellular are connected and coarsened in size compared with the counterparts in Fig. 8(e-g). On closer inspection, some finer precipitates are formed between these structures and the adjacent cellular. According to EDS mapping results shown in Fig. 9(c), the coarsened short-rod structure is

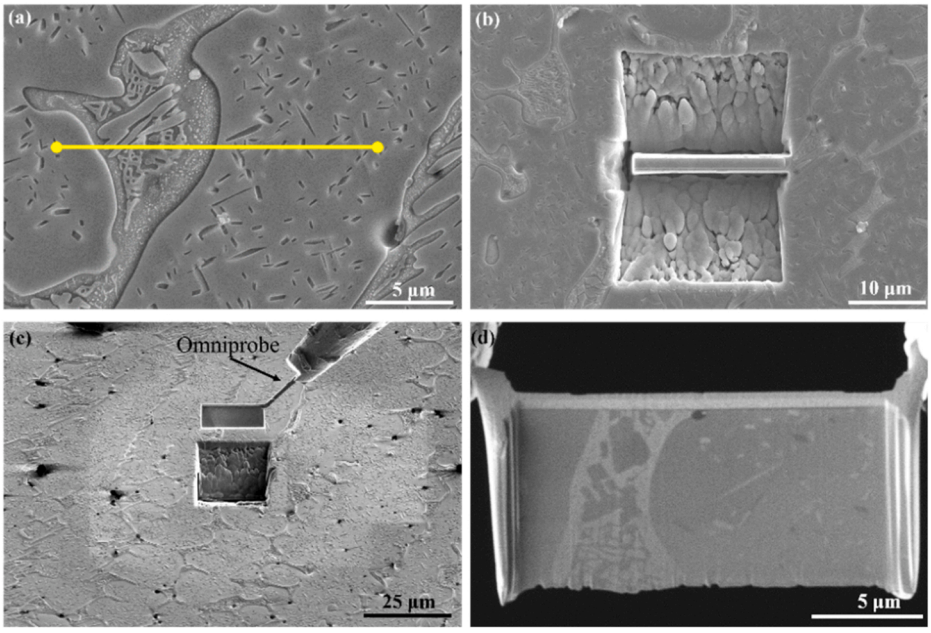

Fig. 10. The preparation of TEM lamella by FIB: (a) sampling location at the area of interest, (b) matter removal above, below, and behind the lamella; (c) lamella cutting, welding, and lift out by the omniprobe; (d) BSE morphology of lamella before final thinning and polishing.

enriched in Cr and Fe but depleted in Ni and Al, which can be identified as FCC structure.

To qualitatively examine the nano precipitates discussed above, TEM lamella was extracted from a typical location revealing the FCC/BCC transition using FIB. Fig. 10(a–c) show the sampling location at the area of interest and the sampling process. Before final thinning and polishing, the morphology of the lamella was captured and shown in Fig. 10(d), showing part of the dendrite core and interdendritic structures with substructures or precipitates inside. After thinning, STEM analysis was conducted to in-depth characterise the nano phases. The bright-field (BF) image of the left-side morphology of the TEM lamella is shown in Fig. 11(a). The contrast of the lower part is different from that of the upper part of the lamella because the residue cut from the sample adheres to and deposits on the bottom during thinning. The EDS mapping results shown in Fig. 11(b) indicate that the matrix of the dendritic core region is more depleted in Al than the interdendritic region, which can be identified as FCC structure [52]. Generally, element content is the main factor that decides the phase structure of HEA since it directly influences valence electron concentration [53]. For $Al_xCoCrFeNi$ HEAs, previous reports exhibit that the phase structure can be different as the fluctuation of chemical composition [54]. The elemental distribution in the interdendritic zone is more complex, which is closer to that in the equimolar AlCoCrFeNi constitution, indicating a more complicated phase transformation is taking place. In the upper region of the interdendritic zone, submicron short-rod structures rich in NiAl are distributed on the FeCr-rich matrix, which can be identified as NiAl-rich B2 precipitating at the FeCr-rich A2 matrix. Similar microstructures have been identified earlier in the vacuum induction melted AlCoCrFeNi HEA [46]. Whether A2 or B2 becomes the matrix highly depends on the local Al content: a comparatively high Al content will prompt B2 to be the matrix and conversely, A2 to act as the matrix [49]. In contrast, the precipitates distributed in the lower part of the interdendrites are more irregular and coarser, and their elemental distribution is very similar to that of the dendrite core (Fig. 11(b) and (c)), which can be considered as an FCC structure. It can be concluded from the EDS results that the A2 phase is NiAl depleted with more Cr concentrated in while the FCC is only Al depleted. Besides, the interface between the dendrite core and interdendritic regions possesses a width range of 500 nm-1 μm. Local chemical composition fluctuation will change the valence electron concentration, which determines the lattice structure of HEAs. Al shows a favourable interaction with other components, particularly strong interactions with Ni and Co [54]. Meanwhile, the self-pair probabilities of Al and Ni tend toward zero during cooling [54], which provides the ordered structure of the NiAl-rich phase. Therefore, a stronger interaction between the Al atom and Ni atom might result in the local segregation of NiAl, which is a classical B2 ordered phase. This phenomenon is also found in the $Al_xCoCrFeNi$ HEA fabricated by other methods, such as casting [55] and laser additive manufacturing [32]. What needs to be highlighted is that this effect will be more prominent as the increase of Al content. The matrix of this region is rich in Ni and Al, which is the B2 phase. More details are shown in Fig. 12.

The TEM results shown in Fig. 12 indicated that the FeCr-rich nanoscale precipitates have spot and rod shapes and are distributed in the AlNi-rich matrix. However, the crystal structures of the spot- and rod-shaped precipitates are different. The HR-TEM image and corresponding FFT pattern shown in Fig. 12(c) of the square zone in Fig. 12(b) show that a different phase with BCC structure precipitated in the ordered B2 matrix (PDF#97–015–0607; Materials Project: mp-1487). Combined with the EDS analysis (Fig. 12(j)), this spot-shaped BCC phase could be associated with the A2 phase with a chemical-disordered BCC structure [55] and an orientation characteristic of $[-111]_{A2}//[001]_{B2}$ and $(0-11)_{A2}//(100)_{B2}$. It can be seen from the FFT pattern shown in Fig. 12(c) that the spacing of {011} in the A2 phase is approximately equal to the spacing of {001} in the B2 phase. However, the other FeCr-rich rod-shaped precipitates contain far less Fe than Cr atoms indicated by the EDS results. In addition, from the FFT pattern of the interface between the rod precipitate and matrix shown in Fig. 12(g), it seems that only the diffractogram of the B2 phase can be recognised at the [010] crystal zone axis. The d-spacing vector distribution shown in Fig. 12(h1) based on the circled spots in the FFT pattern indicated that no significant difference could be found between both sides of the interface. It implies that the spacing of one crystal plane of the nano-rod precipitates equals the {011} of the B2 phase matrix. In addition, the d-spacing vector distribution shown in Fig. 12(h2) of the {001} plane (indicated by arrows in Fig. 12(g)) is the diffraction characteristic of the B2 superlattice. This illustrates that a significant fluctuation existed in the nano-rod zone. Under this circumstance, neither this group of diffracting spots belong to the nano-rod zone nor the group of distant diffract spots of the second phase belong to the B2 phase. With the combinatorial analysis of the crystal plane spacing and EDS result, the

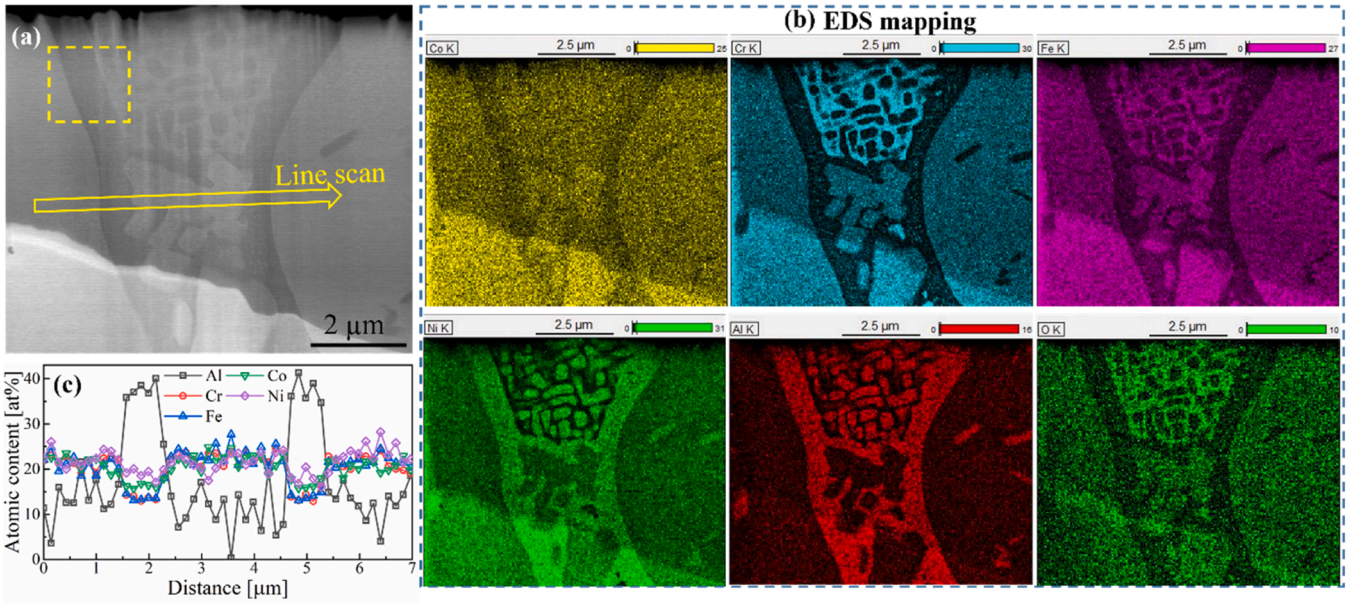

Fig. 11. (a) TEM High-angle annular dark-field (HAADF) image shows the morphology of the left half of the TEM lamella; (b) corresponding EDS elemental mappings; (c) EDS line scan results on the zone indicated in (a) by a yellow hollow arrow.

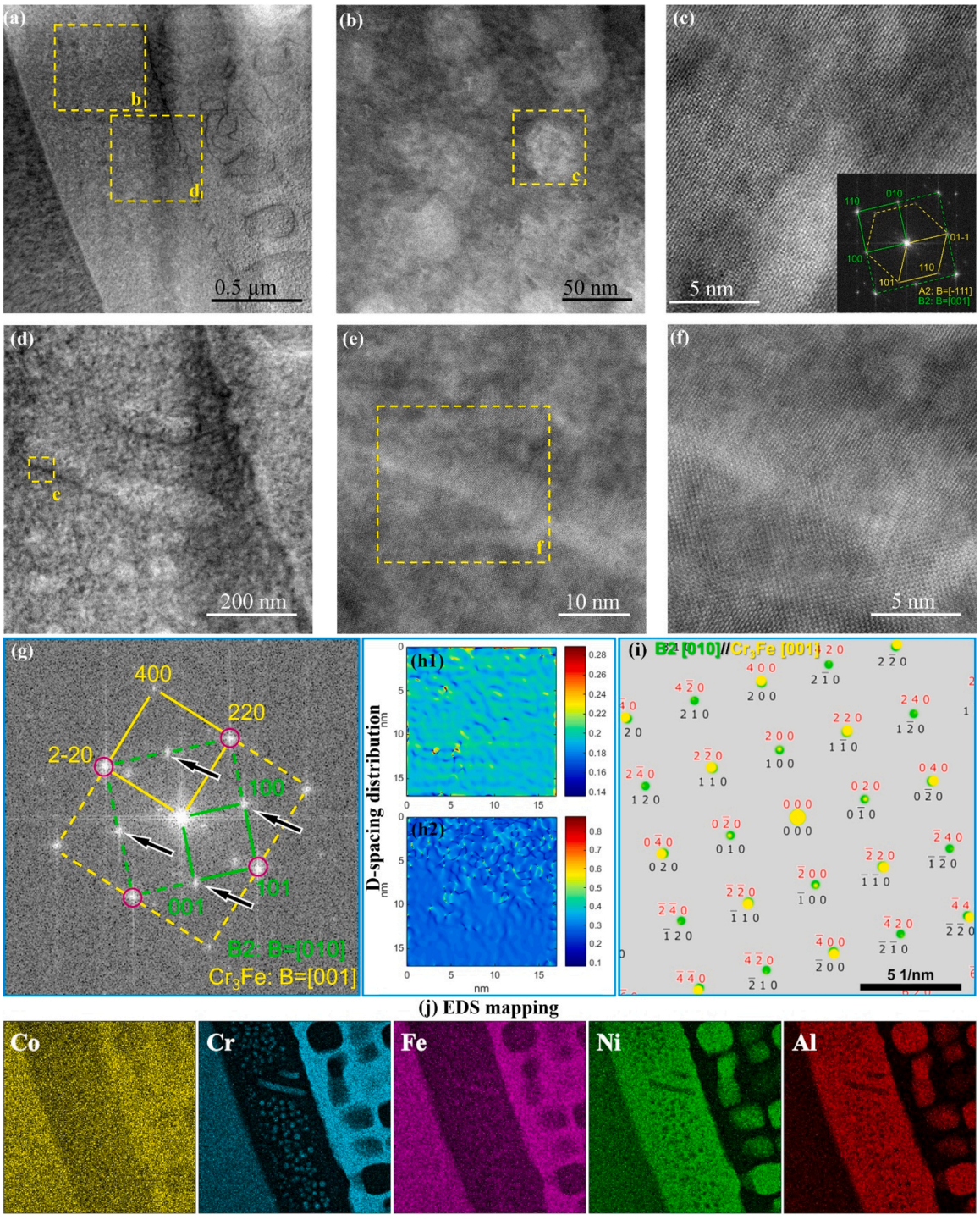

Fig. 12. (a) Bright-field (BF) image displaying the interface between the dendrite core and interdendritic regions labelled by yellow dashed rectangles in Fig. 10(a); (b) HAADF image detail of a; (c) HAADF detail after tilting to cube axis and corresponding diffractogram; (d) BF image taken from the yellow dashed square shown in (a); (e, f) magnified HAADF images of (d); (g) FFT pattern of (f); (h1) D-spacing distribution marked by circles in (f); (h2) D-spacing distribution marked by arrows in (f) FFT pattern; (i) simulated electron diffraction pattern: B2[010]//Cr_3Fe[001]; (j) EDS elemental mappings of (a).

phase structure of the nano-rod zone can be identified as Cr_3Fe intermetallic (PDF#97–018–8261; Materials Project: mp-1008282) with an ordered BCC lattice. Meanwhile, the simulated electron diffraction pattern in Fig. 12(i) indicated that the extinct {001} planes of the Cr_3Fe superlattice would be absent at the direction B = <001 > and the electron diffraction intensities of {002} planes are very weak, which match the FFT pattern in this study. It should be noted that the spacing of the {022} plane of Cr_3Fe is very similar to the {011} plane of the B2 phase. Therefore, the diffraction spots of the {022} plane of Cr_3Fe coincided with the {011} plane of the B2 phase when the {022} plane of Cr_3Fe is parallel to the {011} plane of the B2 phase. Accordingly, the BCC phase in this study can be divided into three different types: the AlNi-rich ordered B2 phase, the FeCr-rich disordered A2 phase, and the ordered Cr_3Fe intermetallic.

Fig. 13(a-d) show the micron-scale AlNi-rich precipitates with rod shapes spread out in the CoCrFe-rich matrix. As indicated from the FFT

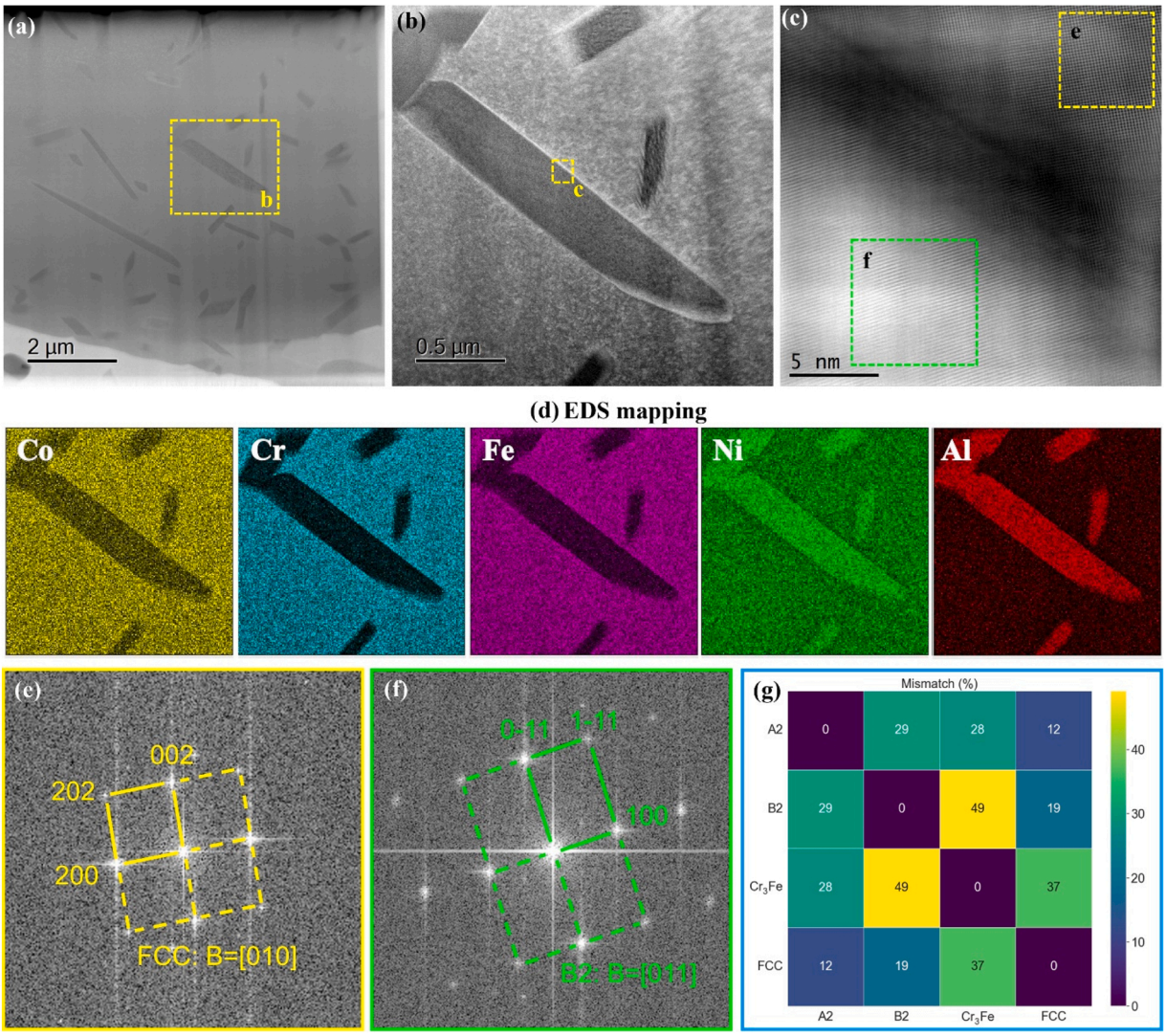

Fig. 13. TEM images of Cr-rich particles precipitated at the grain boundary shown in R1 FIB sample: (a) TEM-HAADF image shows the morphology of the right half of the TEM lamella; (b) BF after tilting the rod on axis - a net tilt difference of only a few degrees; (c) high-resolution transmission electron microscopy (HRTEM) image of the precipitate; (d) EDS elemental mappings of area exhibited in (b); (e) FFT pattern of the yellow rectangular area; (f) FFT pattern of the green rectangular area; (g) mismatch between different phases.

patterns shown in Fig. 13(e) and (f), the CoCrFe-rich matrix possesses an FFT pattern of disordered FCC structure at B = [010] while the AlNi-rich rod precipitates exhibit a BCC structure with the superlattice pattern at B = [011]. Hence, the ordered AlNi-rich B2 phase precipitated at the disordered CoCrFe-rich FCC phase zone at grain boundaries, which resulted in a long-range disordering and short-range ordering characteristic. Furthermore, by calculating the lattice parameters of different phases, the mismatch δ and distance between dislocations D can be obtained and are listed in Table 4 and Fig. 13(g). As indicated, a semi-coherent interface may exist between the FCC phase and A2 phase, owing to the mismatch between the two phases being 12.33 % together with a large dislocation spacing of 28.143 Å. In this case, some dislocations can slip through the phase interface, providing a favourable condition for plastic deformation. With the increase of the Al concentration, the B2 phase gradually replaced the matrix role of the A2 phase in the BCC phase zone. Here, the significant mismatch and low dislocation spacing of the interface between the B2 phase and FCC phase, indicate that an incoherent interface may have formed between the two phases. Therefore, the dislocation movements may be impeded by the phase interfaces, subsequently, abundant dislocations will pile up at the phase interfaces and grain boundaries, leading to the work hardening during plastic deformation. While the BCC phase replaced the matrix role of the FCC phase in the material with the addition of the Al element, the significant mismatch and low dislocation spacing of the incoherent interface between the different BCC phases (involving disordered A2 phase, ordered B2 phase, and ordered Cr_3Fe intermetallic) will even exacerbate work hardening.

Table 4
Mismatch and dislocation distance between different phases.

δ (%)/D (Å)	A2	B2	Cr_3Fe	FCC
A2	-	29.28/9.559	28.05/14.111	12.33/28.143
B2	29.28/9.559	-	49.11/5.699	19.34/14.473
Cr_3Fe	28.05/14.111	49.11/5.699	-	36.92/9.399
FCC	12.33/28.143	19.34/14.473	36.92/9.399	-

4. Discussion

Evolution of phase, microstructure, and mechanical properties with a variation of Al content was obtained. However, the contribution degree of microstructure and phase ratio to strengthening is also influenced by Al concentrations, which will be discussed in detail. There are four main

strengthening mechanisms in polycrystalline materials: solid solution strengthening, grain boundary strengthening, dislocation strengthening, and precipitation strengthening [34]. The mechanisms operate independently, and the YS can be defined as a simple sum of the four individual contributions [56,57]:

$$\sigma_{0.2} = \sigma_0 + \Delta\sigma_S + \Delta\sigma_G + \Delta\sigma_D + \Delta\sigma_p \quad (1)$$

where σ_0 refers to the lattice friction strength of $Al_xCoCrFeNi$, calculated to be 137.65, 137.80, 127.56, and 126.07 MPa corresponding to x value of 0.2, 0.28, 0.53, 0.76, respectively after applying the mixture rule [58]. Also, $\Delta\sigma_s$, $\Delta\sigma_G$, $\Delta\sigma_D$, and $\Delta\sigma_P$ represent the strengthening contributions from solid solution, grain boundary, dislocation, and precipitation, respectively. The contributions of these strengthening mechanisms will be evaluated individually.

4.1. Solid solution strengthening

In this alloy system, the Al, Co, Cr, Fe, and Ni atoms are presented as solid solutions. The atomic radii of Al, Co, Cr, Fe, and Ni are 0.143, 0.125, 0.128, 0.126, and 0.124 nm, respectively. The larger atomic radius of Al resulted in a severer lattice distortion, thereby increasing the resistance to dislocation motion through the crystalline lattice [59]. Here, the $Al_xCoCrFeNi$ HEA can be viewed as pseudo-binary alloys, Al_xY_{1-x} (Y denotes the CoCrFeNi solvent matrix; $0 \leq x \leq 1$). Therefore, a standard model for substitutional solid solution strengthening based upon dislocation-solute elastic interactions can be utilised to evaluate the effects of Al-induced solution strengthening [60]:

$$\Delta\sigma_s = \frac{MGC^{0.5}\left|\frac{\varepsilon_G}{1+0.5|\varepsilon_G|} - 3\varepsilon_a\right|^{3/2}}{700} \quad (2)$$

Here, C represents the Al concentration, which is determined to be 4.85 at %, 6.47 at %, 11.61 at %, and 16.12 at % for $Al_xCoCrFeNi$ with x value of 0.2, 0.28, 0.53, 0.76, respectively. G is the shear modulus of Al, which is 24.13 GPa. M is the Taylor factor, which is 3.06 for FCC and 2.75 for BCC [61]. ε_G and ε_a refer to the mismatches of shear modulus and lattice, respectively. The parameter ε_a can be readily obtained from refined XRD patterns (lattice parameters of $Al_xCoCrFeNi$ with x value of 0.2, 0.28, 0.53, 0.76 are 0.3579 nm, 0.3598 nm, 0.3618 nm, and 0.3618 nm, respectively). Normally, the parameter ε_G is too small to be neglected in comparison to ε_a. In this case, the value of ε_s and thus $\Delta\sigma$ can be effectively estimated. The strength enhancement caused by Al solid-solution hardening in $Al_xCoCrFeNi$ with x value of 0.2, 0.28, 0.53, 0.76 can be subsequently calculated to be 61.6, 68.1, 92.0, and 115.2 MPa, respectively.

4.2. Grain boundary strengthening

Grain boundary strengthening occurs due to the hindering effect of grain boundary on dislocation movement. The smaller the grain, the more grain boundaries, the greater the resistance effect, and the larger the strengthening effect. The effects of grain boundary on the incremental YS ($\Delta\sigma_G$) can be effectively evaluated by the Hall-Petch relationship [62]:

$$\Delta\sigma_G = kd^{-1/2} \quad (3)$$

where k refers to the strengthening coefficient, values of which can be estimated to be 42.6, 42.4, 39.7, and 38.5 MPa·$\mu m^{1/2}$ for $Al_xCoCrFeNi$ with x value of 0.2, 0.28, 0.53, 0.76, respectively, based on the mixture rule [58]; d represents the mean grain size, values of which were determined by SEM to be approximately 1680, 1497, 278, and 142 μm for $Al_xCoCrFeNi$ with x value of 0.2, 0.28, 0.53, 0.76 respectively. Therefore, the value of $\triangle\sigma_G$ for $Al_xCoCrFeNi$ with x value of 0.2, 0.28, 0.53, 0.76 are calculated to be 1.0, 1.1, 2.4, and 3.3 MPa, respectively. Although the increase in Al content resulted in significant refinement of grain size, the overall grain size was still coarse and contributed little to the total strength.

4.3. 4.3 Dislocation strengthening

The high dislocation density in metal is easy to transfer the dislocation movement to form cutting steps, resulting in dislocation entanglement, thus limiting continuous plastic deformation and contributing to the enhancement in YS. The dislocation strengthening contribution to YS can be estimated by the Bailey-Hirsch equation [56]:

$$\left\{\begin{array}{c}\Delta\sigma_D = M\alpha Gb\rho^{0.5} \\ \rho = \frac{2\sqrt{3}\,\varepsilon}{Db}\end{array}\right\} \quad (4)$$

where α is a crystalline-dependent constant, with a value of 0.2 for FCC structure [56]and 0.38 for BCC structure [61]; G refers to the shear modulus, with values of 76.9 GPa for the FCC matrix and 83 GPa for the BCC matrix [63,64]; b is burger vector, with values of 0.255 for FCC structure [56] and 0.248 for BCC structure [61]; ρ refers to the dislocation density; D and ε represent the crystallite size and micro strain, respectively, which can be estimated using the Willamson-Hall method [65]. Combining the Cauchy-type assumption [56] in the case of micro strain, the XRD peak broadening β can be described below:

$$\beta\cos\theta = \frac{K\lambda}{D} + (4\sin\theta) \bullet \varepsilon \quad (5)$$

where K is a constant with an approximate value of 0.9; λ is the wavelength of Cu Kα radiation, which is 0.15409 nm; θ represents the Bragg angle. The ε value can be acquired from the slopes of the fitting lines between βcosθ and 4sinθ, as shown in Fig. S4. According to the above-analysed phase results, an FCC single-phase structure which existed in the regions I and II. With a further increase in Al content, FCC+BCC dual phases appeared in Regions III and IV, with the volume fraction of BCC, determined to be 27.1 % and 87.7 %, respectively. Therefore, combined with the mixing rule, the contribution from dislocation strengthening in YS for $Al_xCoCrFeNi$ with x value of 0.2, 0.28, 0.53, 0.76 can be evaluated as 8.9 MPa, 15.6 MPa, 54.0 MPa, and 88.1 MPa, respectively.

4.4. Precipitation strengthening

Precipitation strengthening is highly correlated to the crystalline structure, lattice constant, microstructure morphology, and size distribution of the precipitates. As discussed, abundant precipitates are distributed in both the BCC and FCC matrix, which are expected to contribute to strengthening. Therefore, the strength enhancement from precipitation in $Al_{0.53}CoCrFeNi$ and $Al_{0.76}CoCrFeNi$ can be estimated using the mixture rule [58]:

$$\Delta\sigma_p = f_{FCC} \bullet \Delta\sigma_{pFCC} + f_{BCC} \bullet \Delta\sigma_{pBCC} \quad (6)$$

where f_{FCC} and f_{BCC} indicate the proportion of the FCC and BCC phases, respectively; $\Delta\sigma_{pFCC}$ and $\Delta\sigma_{pBCC}$ refer to the precipitation strengthening contribution from the FCC and BCC matrices, respectively.

In the FCC matrix, the precipitates' structure often consists of intragranular nanoscale ordered $L1_2$ precipitates which are coherent with the matrix, and grain-boundary B2 precipitates which are semi-coherent or incoherent with the matrix[66], [67]. Also, it has been reported that B2 precipitates are more inclined to be distributed in the vicinity of grain boundaries when $L1_2$ precipitates are highly refined and nucleate homogeneously throughout the matrix grains [67]. The strength contributed by precipitates is affected by the mutual effect between the precipitates and dislocations. In this case, this should follow the Orowan by-pass mechanism once the precipitates surpass a critical value and are incoherent with the matrix, or particle shearing mechanism when the precipitates are coherent and fine [68]. Therefore, the

incoherent B2 precipitates dispersed in the FCC matrix should abide by the Orowan by-pass mechanism [69]:

$$\Delta\sigma_{orw} = M_{FCC}\frac{0.4Gb}{\pi\sqrt{1-\nu}}\frac{\ln(1.633r/b)}{1.633r(\sqrt{\pi/4f}-1)} \quad (7)$$

where M_{FCC} is the Taylor factor of the FCC matrix, which is 3.06 [70], G refers to the shear modulus of the FCC matrix, which is 76.9 GPa [63]; b represents the Burgers vector magnitude with the value of 0.254 nm for the FCC matrix; υ is the Poisson ratio with a value of 0.25; r and f are the average radii and volume fraction of the precipitates, with values of 374 nm and 5.8 %, respectively.

However, for $L1_2$ coherent precipitates sheared by dislocations, its contribution in $\sigma_{0.2}$ mainly derives from coherency strengthening ($\Delta\sigma_{CS}$), modulus strengthening ($\Delta\sigma_{MS}$), and order strengthening ($\Delta\sigma_{OS}$) [63]:

$$\left\{\begin{array}{c}\Delta\sigma_{CS} = M\alpha_{\varepsilon}(0.667G\varepsilon)^{1.5}\left(\frac{rf}{0.5Gb}\right)^{0.5}\\ \Delta\sigma_{MS} = 0.0055M(\Delta G)^{1.5}\left(\frac{2f}{G}\right)^{0.5}\left(\frac{r}{b}\right)^{1.5m-1}\\ \Delta\sigma_{OS} = 0.81M\frac{\gamma_{APB}}{2b}(\frac{3\pi f}{8})^{0.5}\end{array}\right\} \quad (8)$$

where α_{ε} is a constant, 2.6 [63]; ε is the $L1_2$ precipitate / FCC matrix lattice parameter mismatch, which is 0.084 % [71]; ΔG is the $L1_2$ precipitate / FCC matrix shear modulus mismatch, which is 19.2 GPa [72]; m is a constant value of 0.85 [72]; and γ_{APB} is the antiphase boundary energy of the L12 precipitate, with the value of 0.175 J/m^2 [72]; f and r are the volume fraction and mean radius of the $L1_2$ precipitates, with estimated values of 20 % and 10 nm, respectively [73]. Both the $\Delta\sigma_{CS}$ and $\Delta\sigma_{MS}$ take place before shearing and the $\Delta\sigma_{OS}$ occurs during shearing. The total strength increment from the shearing of the precipitates is the larger one between $\Delta\sigma_{CS} + \Delta\sigma_{MS}$ and $\Delta\sigma_{OS}$.

Since the BCC area in these regions mainly consists of A2 and B2 phases, spinodal decomposition strengthening should also be considered [50]. Therefore, the $\triangle\sigma_{pBCC}$ can be expressed as [74]:

$$\left\{\begin{array}{c}\Delta\sigma_{pBCC} = M_{BCC}(\Delta\tau_{SDS} + \Delta\tau_{DOS})\\ \Delta\tau_{SS} = \frac{0.5A\varepsilon E}{1-\nu} + \frac{0.65\Delta Gb}{\lambda}\\ \Delta\tau_{DOS} = 121.2{\gamma_{APB}}^{0.5}f^{0.5}r^{-0.5}\end{array}\right\} \quad (9)$$

where M_{BCC} is the Taylor factor of the BCC matrix, which is 2.73 [64]; $\Delta\tau_{SDS}$ and $\Delta\tau_{DOS}$ represent the critical resolved shear stress generated from the spinodal decomposition and disordered structure, respectively; λ and A are the wavelength and amplitude of the composition modulation with values of 276 nm and 3.1 %, which can be measured from the EDS line scan shown in Fig. 5(d); E is the elastic modulus, 207 GPa [50]; ν is the Poisson's ratio, 0.3 for BCC; ε and $\triangle G$ are the mismatch in lattice parameter and shear modulus for BCC precipitate / B2 matrix, which are 0.69 % and 3 GPa [63], respectively); γ_{APB} is the antiphase boundary energy of the B2 matrix, with the value of 0.8 J/m^2 [75]; f and r are the volume fraction and mean radius of the precipitates, with values of 38 % and 121 nm estimated from the SEM results, respectively. Therefore, the values of $\triangle\sigma_p$ for $Al_{0.2}$CoCrFeNi, and $Al_{0.28}$CoCrFeNi, $Al_{0.53}$CoCrFeNi, $Al_{0.76}$CoCrFeNi can reach 184.0, 184.0, 315.6, and 491.9 MPa, respectively.

Theoretically, the overall strength contributions for $Al_{0.2}$CoCrFeNi, and $Al_{0.28}$CoCrFeNi, $Al_{0.53}$CoCrFeNi, $Al_{0.76}$CoCrFeNi can be summarized as 363, 376, 550, and 820 MPa, respectively. The theoretical strength and experimental strength of different Al compositions are compared in Fig. 14. The discrepancy between the calculated and experimental data is within a reasonable margin of error, which could be ascribed to several factors, including several estimated parameters, irregular morphology of the precipitates, and defects that existed in the as-fabricated status. Nevertheless, through this series of analyses, the evolution in mechanical properties along BD and the factors leading to the changes can be clearly clarified.

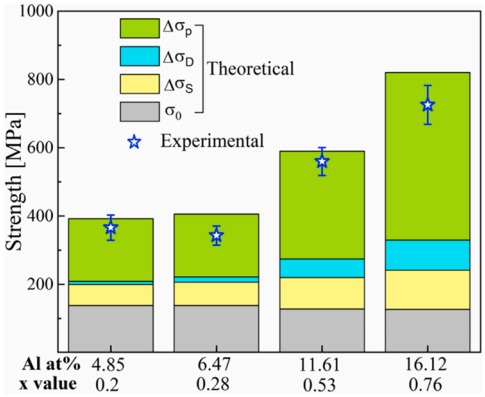

Fig. 14. Comparison between theoretical and experimental strength of Al_xCoCrFeNi with different Al contents.

5. Conclusions

A functionally graded Al_xCoCrFeNi high entropy alloy has been successfully in-situ fabricated using a hybrid PB-WDED approach. The designed variation in Al concentration along the building direction is achieved online by adjusting the Al wire feed speed. The transitions in phase, microstructure, and mechanical performance from bottom to top were systematically discussed and the following conclusions can be made:

(1) The concentration of Al gradually increased to 17 at % while the concentrations of Co, Cr, Fe, and Ni exhibit a downward trend with fluctuations from 25 at % to 21 at % along the deposition height, contributing to a compositional transition from CoCrFeNi with a single FCC structure to $Al_{0.77}$CoCrFeNi with major BCC and minor FCC dual-phase structure. A comparatively continuous transition with slight fluctuation was achieved in the chemical composition benefiting from the remelting and reheating process during the deposition. The peak deflection is striking as Al content increases in the single FCC region while turning to minimal in the dual-phase state.

(2) Room-temperature tensile results indicated that a trend in higher strength and hardening rate but lower plasticity corresponds to with higher Al content. Strength evolution detected along the BD was quantitatively estimated through different strengthening mechanisms. Quantified strengthening in yield strength with different Al concentrations corresponding to each factor was different: precipitation strengthening is predominant, solid-solution hardening and dislocation strengthening cannot be ignored while the grain-boundary strengthening could be negligible.

(3) The growth direction of the FCC columnar in the lower part closely aligns with the < 001 >BD while the counterpart of BCC in the very top region turns to track < 101 >BD. In the BCC grain interior, a combination of interwoven, short-rod, and long-strip FeCr-rich A2 structures is embedded in the NiAl-rich B2 matrix in dark contrast, conforming to the spinodal decomposition mechanism.

(4) In the FCC→BCC transition zone, the columnar crystal size spans from millimetre level to a hundred-micron scale, with BCC dendrites inside growing from dispersing to forming a network, and eventually forming BCC columnar grains as the Al content continues to increase. The dendritic core region is identified as an FCC matrix with micron-scale rod-like B2 precipitates decorated while the interdendritic zone is NiAl-rich B2 precipitating at the FeCr-rich A2 matrix which is closer to that in the equimolar AlCoCrFeNi constitution. Additionally, the interface between the dendrite core and interdendritic regions shows that the

dot-like FeCr-rich disordered A2 phase and rod-like ordered Cr_3Fe intermetallic phase are precipitating at the AlNi-rich ordered B2 phase.

(5) The hybrid PB-WDED technique raised in this investigation demonstrates its capability of directly manufacturing compositionally complex FGM to achieve a unique spacial feature of a ductile end passing to a hard end with a continuous transition, which has great potential in extreme working environments, such as aerospace.

CRediT authorship contribution statement

Ding Jialuo: Writing – review & editing, Supervision, Methodology. **Zhu Lisong:** Writing – review & editing, Software, Investigation, Formal analysis. **Williams Stewart:** Writing – review & editing, Validation, Supervision, Methodology, Formal analysis. **Wang Jun:** Writing – review & editing, Writing – original draft, Methodology, Investigation, Formal analysis, Conceptualization. **Lu Yao:** Writing – original draft, Methodology, Investigation, Formal analysis, Data curation. **Jiang Zhengyi:** Writing – review & editing, Validation, Supervision, Resources, Project administration, Methodology, Funding acquisition, Conceptualization. **Diao Chenglei:** Writing – review & editing, Methodology, Formal analysis.

Declaration of Competing Interest

The authors declare that they have no known competing financial interests or personal relationships that could have appeared to influence the work reported in this paper.

Data availability

Data will be made available on request.

Acknowledgments

This study was financially supported by the Australian Research Council (ARC) ITTC-Rail centre at the University of Wollongong (UOW) and New Wire Additive Manufacturing (NEWAM) United Kingdom program (EP/R027218/1) granted by Engineering and Physical Sciences Research Council. Moreover, the authors also appreciated the equipment support from the research group led by A/ Prof. Zengxi Pan.

Appendix A. Supporting information

Supplementary data associated with this article can be found in the online version at doi:10.1016/j.addma.2023.103424.

References

[1] N. Kashaev, et al., Fatigue behaviour of a laser beam welded CoCrFeNiMn-type high entropy alloy, Mater. Sci. Eng. A vol. 766 (. 2019), https://doi.org/10.1016/j.msea.2019.138358.
[2] Y. Zhang, et al., Microstructures and properties of high-entropy alloys, Prog. Mater. Sci. 61 (2014) 1–93, https://doi.org/10.1016/j.pmatsci.2013.10.001.
[3] M. Wang, et al., A novel bulk eutectic high-entropy alloy with outstanding as-cast specific yield strengths at elevated temperatures, Scr. Mater. vol. 204 (2021), https://doi.org/10.1016/j.scriptamat.2021.114132.
[4] Y. Lu, et al., Ductile and ultrahigh-strength eutectic high-entropy alloys by large-volume 3D printing, J. Mater. Sci. Technol. (2022) 15–21, https://doi.org/10.1016/j.jmst.2022.04.004.
[5] T. Fujieda, et al., CoCrFeNiTi-based high-entropy alloy with superior tensile strength and corrosion resistance achieved by a combination of additive manufacturing using selective electron beam melting and solution treatment, Mater. Lett. vol. 189 (2017) 148–151, https://doi.org/10.1016/j.matlet.2016.11.026.
[6] Y.X. Ye, C.Z. Liu, H. Wang, T.G. Nieh, Friction and wear behavior of a single-phase equiatomic TiZrHfNb high-entropy alloy studied using a nanoscratch technique, Acta Mater. vol. 147 (2018) 78–89, https://doi.org/10.1016/j.actamat.2018.01.014.
[7] B. Schuh, et al., Mechanical properties, microstructure and thermal stability of a nanocrystalline CoCrFeMnNi high-entropy alloy after severe plastic deformation, Acta Mater. vol. 96 (2015) 258–268, https://doi.org/10.1016/j.actamat.2015.06.025.
[8] F. Otto, et al., Decomposition of the single-phase high-entropy alloy CrMnFeCoNi after prolonged anneals at intermediate temperatures, Acta Mater. vol. 112 (2016) 40–52, https://doi.org/10.1016/j.actamat.2016.04.005.
[9] E.J. Pickering, R. Muñoz-Moreno, H.J. Stone, N.G. Jones, Precipitation in the equiatomic high-entropy alloy CrMnFeCoNi, Scr. Mater. vol. 113 (2016) 106–109, https://doi.org/10.1016/j.scriptamat.2015.10.025.
[10] P. Sathiyamoorthi, J. Basu, S. Kashyap, K.G. Pradeep, R.S. Kottada, Thermal stability and grain boundary strengthening in ultrafine-grained CoCrFeNi high entropy alloy composite, Mater. Des. vol. 134 (2017) 426–433, https://doi.org/10.1016/j.matdes.2017.08.053.
[11] S.G. Ma, P.K. Liaw, M.C. Gao, J.W. Qiao, Z.H. Wang, Y. Zhang, Damping behavior of AlxCoCrFeNi high-entropy alloys by a dynamic mechanical analyzer, J. Alloy. Compd. vol. 604 (2014) 331–339, https://doi.org/10.1016/j.jallcom.2014.03.050.
[12] J. Joseph, T. Jarvis, X. Wu, N. Stanford, P. Hodgson, D.M. Fabijanic, Comparative study of the microstructures and mechanical properties of direct laser fabricated and arc-melted AlxCoCrFeNi high entropy alloys, Mater. Sci. Eng. A vol. 633 (2015) 184–193, https://doi.org/10.1016/j.msea.2015.02.072.
[13] W.R. Wang, W.L. Wang, S.C. Wang, Y.C. Tsai, C.H. Lai, J.W. Yeh, Effects of Al addition on the microstructure and mechanical property of Al xCoCrFeNi high-entropy alloys, Intermetallics (Barking) vol. 26 (2012) 44–51, https://doi.org/10.1016/j.intermet.2012.03.005.
[14] G. Jin, M. Takeuchi, S. Honda, T. Nishikawa, H. Awaji, Properties of multilayered mullite/Mo functionally graded materials fabricated by powder metallurgy processing, Mater. Chem. Phys. vol. 89 (2–3) (2005) 238–243, https://doi.org/10.1016/j.matchemphys.2004.03.031.
[15] J.J. Sobczak, L. Drenchev, Metallic functionally graded materials: a specific class of advanced composites, J. Mater. Sci. Technol. vol. 29 (4) (2013) 297–316, https://doi.org/10.1016/j.jmst.2013.02.006.
[16] M. Naebe, K. Shirvanimoghaddam, Functionally graded materials: a review of fabrication and properties, Appl. Mater. Today 5 (2016) 223–245, https://doi.org/10.1016/j.apmt.2016.10.001.
[17] B. Gwalani, et al., Compositionally graded high entropy alloy with a strong front and ductile back, Mater. Today Commun. vol. 20 (2019), https://doi.org/10.1016/j.mtcomm.2019.100602.
[18] P.J. Hazell, Armour: materials, theory, and design.
[19] B. Gwalani, V. Soni, O.A. Waseem, S.A. Mantri, R. Banerjee, Laser additive manufacturing of compositionally graded AlCrFeMoVx (x = 0 to 1) high-entropy alloy system, Opt. Laser Technol. vol. 113 (2019) 330–337, https://doi.org/10.1016/j.optlastec.2019.01.009.
[20] J. Karimi, P. Ma, Y.D. Jia, K.G. Prashanth, Linear patterning of high entropy alloy by additive manufacturing, Manuf. Lett. vol. 24 (2020) 9–13, https://doi.org/10.1016/j.mfglet.2020.03.003.
[21] T. Lehmann, et al., Large-scale metal additive manufacturing: a holistic review of the state of the art and challenges, Int. Mater. Rev. vol. 67 (4) (2022) 410–459, https://doi.org/10.1080/09506608.2021.1971427.
[22] A. Ostovari Moghaddam, N.A. Shaburova, M.N. Samodurova, A. Abdollahzadeh, E. A. Trofimov, Additive manufacturing of high entropy alloys: a practical review, J. Mater. Sci. Technol. 77 (2021) 131–162, https://doi.org/10.1016/j.jmst.2020.11.029.
[23] Y.K. Kim, M.S. Baek, S. Yang, K.A. Lee, In-situ formed oxide enables extraordinary high-cycle fatigue resistance in additively manufactured CoCrFeMnNi high-entropy alloy, Addit. Manuf. vol. 38 (2021), https://doi.org/10.1016/j.addma.2020.101832.
[24] Z. Xu, et al., Microstructure and nanoindentation creep behavior of CoCrFeMnNi high-entropy alloy fabricated by selective laser melting, Addit. Manuf. vol. 28 (2019) 766–771, https://doi.org/10.1016/j.addma.2019.06.012.
[25] H. Zhang, Y. Zhao, S. Huang, S. Zhu, F. Wang, D. Li, Manufacturing and analysis of high-performance refractory high-entropy alloy via selective laser melting (SLM), Materials vol. 12 (5) (2019), https://doi.org/10.3390/ma12050720.
[26] P. Wang, et al., Additively manufactured CoCrFeNiMn high-entropy alloy via pre-alloyed powder, Mater. Des. vol. 168 (2019), https://doi.org/10.1016/j.matdes.2018.107576.
[27] M. Zhang, X. Zhou, D. Wang, L. He, X. Ye, W. Zhang, Additive manufacturing of in-situ strengthened dual-phase AlCoCuFeNi high-entropy alloy by selective electron beam melting, J. Alloy. Compd. vol. 893 (2022), https://doi.org/10.1016/j.jallcom.2021.162259.
[28] K. Kuwabara, H. Shiratori, T. Fujieda, K. Yamanaka, Y. Koizumi, A. Chiba, Mechanical and corrosion properties of AlCoCrFeNi high-entropy alloy fabricated with selective electron beam melting, Addit. Manuf. vol. 23 (2018) 264–271, https://doi.org/10.1016/j.addma.2018.06.006.
[29] B. Xiao, W. Jia, H. Tang, J. Wang, L. Zhou, Microstructure and mechanical properties of WMoTaNbTi refractory high-entropy alloys fabricated by selective electron beam melting, J. Mater. Sci. Technol. vol. 108 (2022) 54–63, https://doi.org/10.1016/j.jmst.2021.07.041.
[30] Y. Bai, et al., Phase transition and heterogeneous strengthening mechanism in CoCrFeNiMn high-entropy alloy fabricated by laser-engineered net shaping via annealing at intermediate-temperature, J. Mater. Sci. Technol. vol. 92 (2021) 129–137, https://doi.org/10.1016/j.jmst.2021.03.028.
[31] H. Dobbelstein, E.L. Gurevich, E.P. George, A. Ostendorf, G. Laplanche, Laser metal deposition of a refractory TiZrNbHfTa high-entropy alloy, Addit. Manuf. vol. 24 (2018) 386–390, https://doi.org/10.1016/j.addma.2018.10.008.
[32] L. Zhu, et al., Strain hardening and strengthening mechanism of laser melting deposition (LMD) additively manufactured FeCoCrNiAl0.5 high-entropy alloy, Mater. Charact. vol. 194 (2022), https://doi.org/10.1016/j.matchar.2022.112365.

[33] J. Wang, et al., Effects of inter-layer remelting frequency on the microstructure evolution and mechanical properties of equimolar CoCrFeNiMn high entropy alloys during in-situ powder-bed arc additive manufacturing (PBAAM) process, J. Mater. Sci. Technol. vol. 113 (2022) 90–104, https://doi.org/10.1016/j.jmst.2021.10.001.
[34] Q. Shen, X. Kong, X. Chen, X. Yao, V.B. Deev, E.S. Prusov, Powder plasma arc additive manufactured CoCrFeNi(SiC)x high-entropy alloys: Microstructure and mechanical properties, Mater. Lett. vol. 282 (2021), https://doi.org/10.1016/j.matlet.2020.128736.
[35] Z. Sun, et al., Reducing hot tearing by grain boundary segregation engineering in additive manufacturing: example of an AlxCoCrFeNi high-entropy alloy, Acta Mater. vol. 204 (2021), https://doi.org/10.1016/j.actamat.2020.116505.
[36] J. Joseph, P. Hodgson, T. Jarvis, X. Wu, N. Stanford, D.M. Fabijanic, Effect of hot isostatic pressing on the microstructure and mechanical properties of additive manufactured AlxCoCrFeNi high entropy alloys, Mater. Sci. Eng. A vol. 733 (2018) 59–70, https://doi.org/10.1016/j.msea.2018.07.036.
[37] M. Li, J. Gazquez, A. Borisevich, R. Mishra, K.M. Flores, Evaluation of microstructure and mechanical property variations in AlxCoCrFeNi high entropy alloys produced by a high-throughput laser deposition method, Intermetallics (Barking) vol. 95 (2018) 110–118, https://doi.org/10.1016/j.intermet.2018.01.021.
[38] M. Klinger, A. Jäger, Crystallographic Tool Box (CrysTBox): automated tools for transmission electron microscopists and crystallographers, J. Appl. Crystallogr vol. 48 (2015) 2012–2018, https://doi.org/10.1107/S1600576715017252.
[39] J. Wang, et al., Characterization of wire arc additively manufactured titanium aluminide functionally graded material: microstructure, mechanical properties and oxidation behaviour, Mater. Sci. Eng. A vol. 734 (2018) 110–119, https://doi.org/10.1016/j.msea.2018.07.097.
[40] T. DebRoy, et al., Additive manufacturing of metallic components – Process, structure and properties, Prog. Mater. Sci. 92 (2018) 112–224, https://doi.org/10.1016/j.pmatsci.2017.10.001.
[41] W.R. Wang, W.L. Wang, S.C. Wang, Y.C. Tsai, C.H. Lai, J.W. Yeh, Effects of Al addition on the microstructure and mechanical property of Al xCoCrFeNi high-entropy alloys, Intermetallics (Barking) vol. 26 (2012) 44–51, https://doi.org/10.1016/j.intermet.2012.03.005.
[42] G.M. Karthik, S. Panikar, G.D.J. Ram, R.S. Kottada, Additive manufacturing of an aluminum matrix composite reinforced with nanocrystalline high-entropy alloy particles, Mater. Sci. Eng. A vol. 679 (2017) 193–203, https://doi.org/10.1016/j.msea.2016.10.038.
[43] B. Gwalani, S. Gangireddy, Y. Zheng, V. Soni, R.S. Mishra, R. Banerjee, Influence of ordered L1 2 precipitation on strain-rate dependent mechanical behavior in a eutectic high entropy alloy, Sci. Rep. vol. 9 (1) (2019), https://doi.org/10.1038/s41598-019-42870-y.
[44] D.D. Zhang, J.Y. Zhang, J. Kuang, G. Liu, J. Sun, The B2 phase-driven microstructural heterogeneities and twinning enable ultrahigh cryogenic strength and large ductility in NiCoCr-based medium-entropy alloy, Acta Mater. vol. 233 (2022), https://doi.org/10.1016/j.actamat.2022.117981.
[45] M. Garibaldi, I. Ashcroft, M. Simonelli, R. Hague, Metallurgy of high-silicon steel parts produced using selective laser melting, Acta Mater. vol. 110 (2016) 207–216, https://doi.org/10.1016/j.actamat.2016.03.037.
[46] C. Zhao, et al., Optimizing mechanical and magnetic properties of AlCoCrFeNi high-entropy alloy via FCC to BCC phase transformation, J. Mater. Sci. Technol. vol. 86 (2021) 117–126, https://doi.org/10.1016/j.jmst.2020.12.080.
[47] D. Karlsson, et al., Binder jetting of the AlCoCrFeNi alloy, Addit. Manuf. vol. 27 (2019) 72–79, https://doi.org/10.1016/j.addma.2019.02.010.
[48] D. Karlsson, et al., Elemental segregation in an AlCoCrFeNi high-entropy alloy – a comparison between selective laser melting and induction melting, J. Alloy. Compd. vol. 784 (2019) 195–203, https://doi.org/10.1016/j.jallcom.2018.12.267.
[49] Y. Ma, et al., The BCC/B2 morphologies in AlxNiCoFeCr high-entropy alloys, Metals (Basel) vol. 7 (2) (2017), https://doi.org/10.3390/met7020057.
[50] Q. Tian, G. Zhang, K. Yin, W. Wang, W. Cheng, Y. Wang, The strengthening effects of relatively lightweight AlCoCrFeNi high entropy alloy, Mater. Charact. vol. 151 (2019) 302–309, https://doi.org/10.1016/j.matchar.2019.03.006.
[51] A. Manzoni, H. Daoud, R. Völkl, U. Glatzel, N. Wanderka, Phase separation in equiatomic AlCoCrFeNi high-entropy alloy, Ultramicroscopy vol. 132 (2013) 212–215, https://doi.org/10.1016/j.ultramic.2012.12.015.
[52] E. Strumza, V. Ezersky, E. Brosh, M. Aizenshtein, S. Hayun, A comprehensive study of phase transitions in Al0.5CoCrFeNi high-entropy alloy at intermediate temperatures ($400 \leq T \leq 900\ ^{\circ}C$) (Mar), J. Alloy. Compd. vol. 898 (2022), https://doi.org/10.1016/j.jallcom.2021.162955.
[53] W.H. Liu, et al., Unveiling the electronic origin for pressure-induced phase transitions in high-entropy alloys, Matter vol. 2 (3) (2020) 751–763, https://doi.org/10.1016/j.matt.2019.12.023.
[54] L.J. Santodonato, P.K. Liaw, R.R. Unocic, H. Bei, J.R. Morris, Predictive multiphase evolution in Al-containing high-entropy alloys, Nat. Commun. vol. 9 (1) (2018), https://doi.org/10.1038/s41467-018-06757-2.
[55] M. Kang, K.R. Lim, J.W. Won, Y.S. Na, Effect of Co content on the mechanical properties of A2 and B2 phases in AlCoxCrFeNi high-entropy alloys, J. Alloy. Compd. vol. 769 (2018) 808–812, https://doi.org/10.1016/j.jallcom.2018.07.346.
[56] J.Y. He, et al., A precipitation-hardened high-entropy alloy with outstanding tensile properties, Acta Mater. vol. 102 (2016) 187–196, https://doi.org/10.1016/j.actamat.2015.08.076.
[57] J.Y. He, et al., Effects of Al addition on structural evolution and tensile properties of the FeCoNiCrMn high-entropy alloy system, Acta Mater. vol. 62 (1) (2014) 105–113, https://doi.org/10.1016/j.actamat.2013.09.037.
[58] R. Sriharitha, B.S. Murty, R.S. Kottada, Alloying, thermal stability and strengthening in spark plasma sintered AlxCoCrCuFeNi high entropy alloys, J. Alloy. Compd. vol. 583 (2014) 419–426, https://doi.org/10.1016/j.jallcom.2013.08.176.
[59] Y.D. Wu, et al., Phase composition and solid solution strengthening effect in TiZrNbMoV high-entropy alloys, Mater. Des. vol. 83 (2015) 651–660, https://doi.org/10.1016/j.matdes.2015.06.072.
[60] G. Qin, et al., An as-cast high-entropy alloy with remarkable mechanical properties strengthened by nanometer precipitates, Nanoscale vol. 12 (6) (2020) 3965–3976, https://doi.org/10.1039/c9nr08338c.
[61] Z.J. Xie, et al., Characterization of nano-sized precipitation and dislocations and the correlation with mechanical properties of a low alloy TRIP-aided steel, Mater. Sci. Eng. A vol. 763 (2019), https://doi.org/10.1016/j.msea.2019.138149.
[62] W.H. Liu, Y. Wu, J.Y. He, T.G. Nieh, Z.P. Lu, Grain growth and the Hall-Petch relationship in a high-entropy FeCrNiCoMn alloy, Scr. Mater. vol. 68 (7) (2013) 526–529, https://doi.org/10.1016/j.scriptamat.2012.12.002.
[63] S. il Baik, S.Y. Wang, P.K. Liaw, D.C. Dunand, Increasing the creep resistance of Fe-Ni-Al-Cr superalloys via Ti additions by optimizing the B2/L21 ratio in composite nano-precipitates, Acta Mater. vol. 157 (2018) 142–154, https://doi.org/10.1016/j.actamat.2018.07.025.
[64] Y. Ma, et al., Controlled formation of coherent cuboidal nanoprecipitates in body-centered cubic high-entropy alloys based on Al2(Ni,Co,Fe,Cr)14 compositions, Acta Mater. vol. 147 (2018) 213–225, https://doi.org/10.1016/j.actamat.2018.01.050.
[65] G.K. Williamsont and W.H. Hallt, X-Ray Line Broadening from Filed Aluminium and Wolfram.
[66] Y. He, et al., Enhancing mechanical properties of Al0.25CoCrFeNi high-entropy alloy via cold rolling and subsequent annealing, J. Alloy. Compd. vol. 830 (2020), https://doi.org/10.1016/j.jallcom.2020.154645.
[67] B. Gwalani, V. Soni, M. Lee, S.A. Mantri, Y. Ren, R. Banerjee, Optimizing the coupled effects of Hall-Petch and precipitation strengthening in a Al0.3CoCrFeNi high entropy alloy, Mater. Des. vol. 121 (2017) 254–260, https://doi.org/10.1016/j.matdes.2017.02.072.
[68] N.Q. Vo, C.H. Liebscher, M.J.S. Rawlings, M. Asta, D.C. Dunand, Creep properties and microstructure of a precipitation-strengthened ferritic Fe-Al-Ni-Cr alloy, Acta Mater. vol. 71 (2014) 89–99, https://doi.org/10.1016/j.actamat.2014.02.020.
[69] K. Ma, et al., Mechanical behavior and strengthening mechanisms in ultrafine grain precipitation-strengthened aluminum alloy, Acta Mater. vol. 62 (1) (2014) 141–155, https://doi.org/10.1016/j.actamat.2013.09.042.
[70] R.E. Stoller and S.J. Zinkle, Section 4. Mechanical behavior of irradiated materials On the relationship between uniaxial yield strength and resolved shear stress in polycrystalline materials. [Online]. Available: www.elsevier.nl/locate/jnucmat.
[71] I. v Kireeva, Y.I. Chumlyakov, Z. v Pobedennaya, A. v Vyrodova, Effect of γ′-phase particles on the orientation and temperature dependence of the mechanical behaviour of Al0.3CoCrFeNi high-entropy alloy single crystals, Mater. Sci. Eng. A vol. 772 (2020), https://doi.org/10.1016/j.msea.2019.138772.
[72] J.-S. Wang, Dislocation Nucleation and the Intrinsic Fracture Behavior Of L1 2 Intermetallic Alloys.
[73] B. Gwalani, et al., Modifying transformation pathways in high entropy alloys or complex concentrated alloys via thermo-mechanical processing, Acta Mater. vol. 153 (2018) 169–185, https://doi.org/10.1016/j.actamat.2018.05.009.
[74] Q. Fan, et al., AlCoCrFeNi high-entropy alloy coatings prepared by gas tungsten arc cladding: Microstructure, mechanical and corrosion properties, Intermetallics (Barking) vol. 138 (2021), https://doi.org/10.1016/j.intermet.2021.107337.
[75] M. Feuerbacher, Dislocations and deformation microstructure in a B2-ordered Al 28 Co 20 Cr 11 Fe 15 Ni 26 high-entropy alloy, Sci. Rep. vol. 6 (2016), https://doi.org/10.1038/srep29700.

2023-01-23

Additive manufacturing of a functionally graded high entropy alloy using a hybrid powder-bed wire-based direct energy deposition approach

Lu, Yao

Elsevier

Lu Y, Wang J, Williams S, et al., (2023) Additive manufacturing of a functionally graded high entropy alloy using a hybrid powder-bed wire-based direct energy deposition approach, Additive Manufacturing, Volume 63, February 2023, Article number 103424

https://doi.org/10.1016/j.addma.2023.103424